Evolution of a Florida Thunderstorm during the Convection and Precipitation/ Electrification Experiment: The Case of 9 August 1991

V. N. BRINGI,* K. KNUPP,† A. DETWILER,# L. LIU,@ I. J. CAYLOR,& AND R. A. BLACK**

*Colorado State University, Fort Collins, Colorado
†University of Alabama in Huntsville, Huntsville, Alabama
#South Dakota School of Mines and Technology, Rapid City, South Dakota
@South China University of Technology, Guangzhou, China
&Science Systems and Applications, Inc., Lanham, Maryland
**NOAA/AOML, Miami, Florida

(Manuscript received 27 October 1995, in final form 13 November 1996)

ABSTRACT

The relationships among kinematic, microphysical, and electric field properties within a multicell Florida thunderstorm are investigated using observations from three Doppler radars (one with multiple wavelength and polarization diversity capabilities), four instrumented penetrating aircraft, a surface-based electric field mill network, and other observation facilities. The storm was convectively active for about 1 h and at least five primary cells developed within the storm during this time, one of which went through three consecutive development cycles. The updrafts in this storm were 2–4 km wide, exhibited bubble-like evolution, and had lifetimes of 10–20 min. The maximum updraft determined by the multiple Doppler analysis was about 20 m s^{-1}. A differential reflectivity (Z_{DR}) ''column,'' indicating regions containing millimeter-size raindrops, extending above the freezing level, was associated with each cell during its developing stages. This column reached altitudes exceeding 6 km (−8°C) in the stronger updrafts. As the Z_{DR} columns reached maximum altitude, a ''cap'' of enhanced linear depolarization ratio (LDR) and enhanced 3-cm wavelength attenuation (A_3) formed, overlapping the upper regions of the Z_{DR} column. These parameters indicate rapid development of mixed-phase conditions initiated by freezing of supercooled raindrops.

Lightning was observed only in the central and strongest convective cell. Electric fields exceeding 10 kV m^{-1} were noted during aircraft penetrations in this as well as several other cells that did not produce lightning. Fields exceeding 1 kV m^{-1} were noted by the instrumented aircraft at midcloud levels within a few minutes of development of mixed-phase conditions at these levels or aloft. The first intracloud lightning was detected by the surface field mill network within 5 min of development of mixed-phase conditions aloft in the first cycle of development in the central cell, and the first cloud-to-ground event was noted within 9 min of this development. Lightning continued through two additional cycles of updraft growth in this central region and diminished as the convection subsided after about 30 min. Aircraft-measured electric fields and lightning retrievals from the surface field meter network are consistent with a tendency for negative charge to accumulate above the 6.5 km (−12°C) level within regions of radar reflectivity maxima and for positive charge to accumulate in the anvil region well above 9 km (−30°C).

1. Introduction

One broad objective of the Convection and Precipitation–Electrification (CaPE) experiment was to identify the relationships among the coevolving wind, water, and electric fields within convective clouds. The CaPE experiment was conducted in east central Florida during the period 8 July–18 August 1991. On 9 August, a multicell storm was the target of intensive observations by four instrumented aircraft, three Doppler radars (one of which had multiparameter measurement capability), and the Kennedy Space Center surface field mill network. It was the only case during CaPE where four aircraft made coordinated, multiple-level penetrations covering the early to mature phase of a multicell storm. The storm location with respect to the three National Center for Atmospheric Research (NCAR) radars (CP-2, CP-3, and CP-4) was suitable for retrieval of wind vectors using multiple-Doppler synthesis.

In this paper we synthesize measurements from various platforms to afford a coherent picture of the coevolving wind, precipitation, and electric fields within identifiable cells of a multicell storm over a duration of approximately 30 minutes. Preliminary analysis of this case can be found in Bringi et al. (1993) and Bringi et al. (1995). Two cells, penetrated by the four aircraft at various stages of their evolution, are analyzed in detail focusing on the vertical structures of multiparameter

Corresponding author address: Dr. V. N. Bringi, Department of Electrical Engineering, Colorado State University, Fort Collins, CO 80523.
E-mail: bringi@engr.colostate.edu

radar measurements (Z_{DR}— differential reflectivity, LDR— linear depolarization ratio, and A_3— specific attenuation at wavelength of 3 cm), updraft magnitudes, and in situ measurements of cloud microphysics (cloud water, hydrometeor images) and electric fields. Several key aircraft penetrations are analyzed during the vigorous growth and the mature phase of these cells. This paper reports on the first observations of this kind involving coordinated multiparameter radar measurements with multiple level in-cloud aircraft for verification of radar signatures.

There have been relatively few studies in the past that combine multiparameter radar with multiple-Doppler data, and, to the best of our knowledge, none with supporting in-cloud aircraft data. Tuttle et al. (1989) were the first to show the collocation of the positive Z_{DR} column with the updraft core in an isolated, microburst-producing storm in northern Alabama. Bringi et al. (1991) reported on low-altitude (2.7 km MSL) aircraft penetrations of positive Z_{DR} columns in warm-based clouds in northern Alabama and provided evidence of large drops (up to 7-mm diameter at 10°C) at low concentrations that were coincident with updrafts. They also reported on enhanced values of A_3 near the top of these columns, as well as on the evolution of raindrop spectra from ''growth'' type to equilibrium type at the aircraft penetration altitude (Illingworth 1988). Enhanced LDR (≥ -20 dB) values were found near the top of positive Z_{DR} columns in central Alabama by Herzegh and Jameson (1992), who interpreted the signature as due to tumbling graupel/frozen drops in wet growth. Similar observations also were noted by Bringi et al. (1996) in an intense storm in Colorado. In one case during CaPE, Smith et al. (1995) obtained in situ photographs of a partially freezing raindrop near a region of enhanced LDR in a thunderstorm, confirming that freezing raindrops could also produce LDR ≥ -20 dB. Yuter and Houze (1995a), in a Doppler and multiparameter study of multicellular convection along a sea-breeze front on another day during CaPE, noted a bubble-like evolution of updrafts with vigorous upper-level downdrafts flanking the bubble-like updraft maxima as they reached the upper portion of the storms. These upper-level circulation features were not resolved in the earlier studies of Florida thunderstorms by Byers and Braham (1949). Yuter and Houze also noted that Z_{DR} columns rising well above the freezing level were associated with the updrafts during the early portions of storm evolution, indicating supercooled rain being carried aloft. But later in the storm life cycle they found little evidence for supercooled rain even in very active cells with strong updrafts.

Observational and laboratory evidence suggests a strong link between mixed-phase microphysics and cloud electrification (Williams et al. 1991). A few studies in the past have used multiparameter radar–deduced microphysics combined with surface instrumentation for monitoring electrification to explore this link. Goodman et al. (1988) analyzed lightning production and precipitation evolution within the 20 July 1986 microburst-producing storm in northern Alabama referred to earlier (Tuttle et al. 1989). They found that intracloud lightning began 4 min after the first radar indications of graupel/hail aloft, with the first cloud-to-ground lightning beginning 5 min after that. The peak lightning flash rate came just prior to collapse of the updraft, with 95% of the storm's total flashes being intracloud. Jameson et al. (1996) recently used multiparameter CP-2 radar observations from CaPE to study the onset of electrification (via surface field mill data), and they suggest that the development of positive Z_{DR} columns with enhanced LDR ''caps'' correlates well with the onset of electrification in the three storms they analyzed. Ramachandran et al. (1996) and French et al. (1996) report on other CaPE cases using CP-2 radar and T-28 aircraft observations of thunderstorm cells. They found that a low concentration of raindrops initially develops in the updraft, which in vigorous cells are lofted upward where they freeze between $-5°$ and $-10°$C (Smith et al. 1995), followed by electric field increases and lightning.

Observations presented here provide quantitative results concerning the coevolution of winds, precipitation, and electrification. It is the first study that combines (multiple-Doppler derived) vector winds with Z_h, Z_{DR}, LDR, and A_3, in coordination with multiple-level aircraft penetrations of storm cells. Because of very accurate navigation on the aircraft, a detailed comparison of hydrometeor images with radar signatures is possible during the cell's temporal evolution. Scattering computations from canted, partially freezing raindrops are shown here for the first time and are consistent with the observations of enhanced LDR ≥ -20 dB and modest Z_{DR} (1–2 dB) atop updrafts where frozen drops were observed. In this paper we present the first hydrometeor images obtained in situ during the vigorous growth phase of a cell characterized by positive Z_{DR} columns with an enhanced LDR/A_3 cap overlapping with the column top.

Section 3 gives a brief environmental overview, followed by an overview of the storm structure and evolution. Specific analyses of storm structure during the early growth phase (section 4), vigorous growth phase (section 5), and mature phase (section 6) integrate measurements from the various sensors and relate storm electrification to observed kinematic and microphysical properties. Finally, section 7 synthesizes the microphysical, kinematic, and electrical observations of the various cells. Appendix A provides details of Doppler and multiparameter radar analysis procedures and multiparameter data interpretation, while appendix B provides a brief description of the aircraft and airborne electric field measurements.

2. Analysis procedures and data attributes

The primary database available for this analysis includes 17 penetrations from four aircraft, CP-2 volume

TABLE 1. Summary of aircraft penetration data.

No.	Penetration time (distance)*	A/c	Alt./T (km/°C)	Downdraft (m s^{-1})	Cloud water (g m^{-3})	$\lvert E_z \rvert$ (kV m^{-1})	Max. particle size (mm)	Particle type
Cell A, A′								
1 (cell A)	1805:00–1805:20 (0.4)	P-3	6.5/−11	9.7/0	2.5	0	0.8	drops
2 (cell A)	1809:37–1810:20 (0.5)	P-3	6.5/−10	12.5/−3.3	3.4	2	3.5	rough graupel, drops, frozen drops
3 (A′)	1820:50–1821:20 (0.2)	P-3	6.5/−11	5.5/−10	1.8	16	2.5	rough graupel
4 (A′)	1827:30–1828:15 (0.55)	T28	5.1/−4	0/−7.3	0.1	41	3.6	rough graupel
5 (A′)	1828:15–1829:00 (0.4)	P-3	6.5/−13	7.1/0	1.5	21	3.2	rough graupel
Cell B								
1a	1758:30–1759:05 (0.6)	NKA	5.5/−6	10/−3	2.0	0	3.0	drops, rough graupel
1b	1759:00–1759:30 (0)	WKA	4.0/3	1/−3	1.0	—	4.5	drops
2a	1804:30–1805:00 (1.65)	NKA	5.5/−6	—	0.20	<0.5	2.2	rough graupel
2b	1805:10–1805:30 (0.88)	WKA	4.0/3	0/−3	0.50	—	4.5	smooth graupel
3	1805:30–1805:50 (0.55)	P-3	6.5/−11	4/−8.8	1.0	<0.5	3.0	rough graupel
Cell D								
1	1804:20–1804:45 (0)	WKA	4.0/3	16/0	1.9	—	5.0	drops
2a	1807:35–1808:05 (0.55)	NKA	5.5/−6	12/0	1.70	<0.3	4.0	drops
2b	1808:20–1808:55 (0.22)	WKA	4.0/2.5	12/0	2.20	—	8.0	drops
3a	1810:50–1811:20 (0.33)	NKA	5.5/−6	—	0.20	<0.5	4.0	frozen drops, smooth graupel
3b	1811:25–1811:45 (0.27)	WKA	4.0/2.3	1/0	0	—	7.5	smooth graupel
4	1815:40–1816:10 (0.4)	NKA	5.5/−6.5	0.5/−2	0	5	3.2	rough graupel
5	1815:10–1815:40 (0.55)	P-3	6.5/−11	4/−3	0.20	20	2.5	rough graupel

*Approximate distance (km) from aircraft track to peak reflectivity of cell at aircraft altitude.

scans [acquired primarily in RHI (range–height indicator) mode] available every 2 min, and 15 multiple Doppler analyses (using CP-2, CP-3, and CP-4), available at 2–5-min intervals over the period 1750–1835 UTC. Appendixes A and B outline details of the multiple Doppler–multiparameter radar analyses and aircraft data characteristics.

Time–height sections of radar and in situ aircraft measurements are used in sections 4 and 5 to define individual cell kinematic (w), microphysical (e.g., Z_h, Z_{DR}, LDR, and A_3), and electric field properties. Such detailed observations of the time evolution of a convective cell have not been reported previously. For each volume of radar data a vertical ''box'' is subjectively drawn around the cell (see appendix A), and the multiparameter variables within 3 dB of the peak Z_h at each altitude (from 1.5 to 10.5 km) are averaged to obtain a table of values as a function of height. This procedure is repeated for each volume of data at approximately 3-min intervals and then contoured, resulting in time–height contours of the multiparameter radar variables (and a number of derived parameters as explained in appendix A). The derived parameters obtained from Z_h and Z_{DR} are estimates of ice water content IWC (g m^{-3}) and liquid rain water content LWC (g m^{-3}), as well as vertically integrated total ice water content TIWC (kg) within the cell and the rain mass flux RM (kg s^{-1}) at the 2-km level. For the vertical wind variable (w), the maximum value at each level within the box is chosen and then contoured. One main reason for choosing the reflectivity core region at each height for the time–height sections is related to errors in Z_{DR} and LDR caused by mismatched antenna patterns in regions of large Z_h gradients. Choosing the core region minimizes these errors. Also, estimates of A_3 are very noisy away from the core region, and mismatched antenna patterns also cause error in Z_h gradients. Other methods, for example, contoured frequency by altitude diagrams (CFADs), offer a different approach to studying cell structure (Yuter and Houze 1995a,b).

The four aircraft (NKA, WKA, P-3, and T28) made 17 penetrations of the cells A (followed by A′), B, and D over 35 min during their evolution. The NKA, T-28, and P-3 were instrumented for electrical as well as microphysical measurements (see appendix B). Only the simplest idea of storm structure was available to the aircraft pilots and radar operators in real time during operations. Locations of updrafts, Z_{DR} columns, etc., could not be precisely targeted. Thus, each aircraft penetration may not intercept precisely the most interesting regions of the cells at a given time. Table 1 shows a summary of the aircraft penetration data for cells A, A′, B, and D. The up- and downdraft speeds are peak values, as are cloud water and the magnitude of the vertical electric field component, $\lvert E_z \rvert$. Key parameters measured by aircraft are superimposed on time–height contour diagrams for cells B, A (followed by A′), and D (Figs. 4, 5, and 7). Table 1 also lists the minimum distance from the aircraft track to the location of peak Z_h in the cell at the aircraft altitude. Thus, Table 1 should be

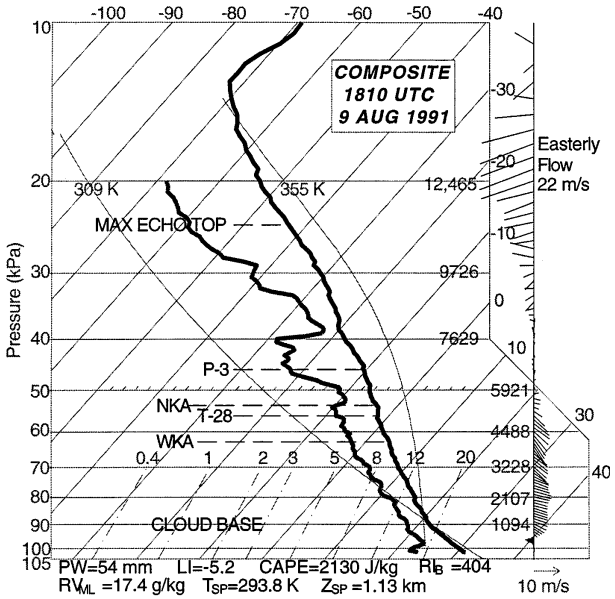

FIG. 1. Representative composite sounding plotted on a skew T–log$p$ diagram, for 1810 UTC 9 August 1991. The height of pressure surfaces is labeled in meters on the right. Reference dry (θ) and saturated (θ_e) adiabats are labeled 309 and 355 K, respectively. The composite is derived from two soundings, a fixed based system (at Tyco airport) and mobile system (NCAR mobile CLASS) located in Fig. 2. A definition of sounding parameters plotted at the bottom is as follows: PW is precipitable water (mm), LI is lifted index (°C), CAPE is convective available potential energy (J kg^{-1}), RI_B is bulk Richardson number, RV_{ML} is mean water vapor mixing ratio in the mixed layer (g kg^{-1}), and T_{sp} and Z_{sp} are temperature (K) and height (km) of the saturation point based on mean values of potential temperature and water vapor in the mixed layer.

consulted when referring to other figures that deal with aircraft data.

We present detailed observations of individual convective cells at three representative stages of cell evolution. Observations of cell B illustrate conditions in an early cell within a multicellular thunderstorm complex. These cells are often weaker than cells that develop later in the storm cycle. Observations of cells A and D are presented for periods of vigorous growth during a period when the storm was actively growing and beginning to produce lightning, while later observations of cells A and A′ are presented to characterize the mature period in storm evolution when lightning is continuing but convection is steady or beginning to decay.

3. Environmental and radar overviews

a. Storm environment

The synoptic setting at 1200 UTC was dominated by relative high pressure over Florida and the Southeast. A representative sounding (Fig. 1) reveals abundant moisture (54-mm precipitable water) and moderate instability (CAPE ~ 2100 J kg^{-1}). Relatively weak (3–6 m s^{-1}) and uniform west to northwesterly winds over the layer 90–60 kPa resulted from flow around the north side of weak high pressure located just to the southwest of Florida. In the upper troposphere an east–west ridge was centered over Alabama, resulting in rather brisk easterly flow over the CaPE region peaking at about 20 m s^{-1} near 20 kPa. Vertical shear of the horizontal wind was largest near the surface where easterly flow associated with the East Coast sea breeze was capped by the prevailing synoptic-scale westerly flow at midlevels, as well as near 30 kPa where the easterly flow was enhanced. The shear vector is thus directed toward the southeast at lower levels and to the west to northwest above 60 kPa. This upper-level shear zone resulted in the ''shearing off'' of cumulus towers that penetrated to this level.

b. Storm structure and evolution

The multicell storm developed to the north of a more extensive (but weakening) multicell complex as shown in Fig. 2 at 1755 UTC (or 1355 EDT). Henceforth, all times will be UTC and all altitudes will be above mean sea level (MSL) unless otherwise specified. This storm consisted of about 10 identifiable cells over its 50-min lifetime. Characteristics of five major cells are listed in order of convective intensity in Table 2. The characteristics chosen to describe the cells in Table 2 are admittedly somewhat subjective, for example, the choice of peak values and altitudes for radar-derived quantities, rather than average or most probable values. However, when Table 2 is combined with Table 1, which gives other physical characteristics such as updrafts, cloud water, etc., it is possible to infer cell characteristics in a more meaningful manner. We attempt to do this here and in later sections.

The cell-naming convention is arbitrary. Cell B in Fig. 2, the initial cell of the storm, was triggered near the intersection of an outflow boundary generated by the large multicell complex to the south and the east coast sea breeze.

Figures 3a–g present a time sequence of constant-altitude (5 km, −3°C) PPI (plan position indicator) sections from 1758–1827. Corresponding vertical sections along a constant Y value marked in Figs. 3a–g are shown in Figs. 3a′–g′. Here the cell-relative vector wind in this constant Y plane is shown. The time series in Fig. 3 clarifies the evolution of five cells, including the most significant one (A, A′), which produced strong electric fields and lightning.

At 1758 cell B (Fig. 3a) exhibits peak Z_h and peak w at 5-km altitude of 40.8 dBZ and 14.1 m s^{-1}, respectively. The vertical section in Fig. 3a′ reveals a positive Z_{DR} column extending up to 6.5 km (−11°C), nearly coincident with the updraft column. The cell at this time is clearly in a vigorous growth phase. During the growth phase of all cells considered, updrafts and Z_{DR} columns were virtually coincident, a pattern contrary to the offset observed by Yuter and Houze (1995b)

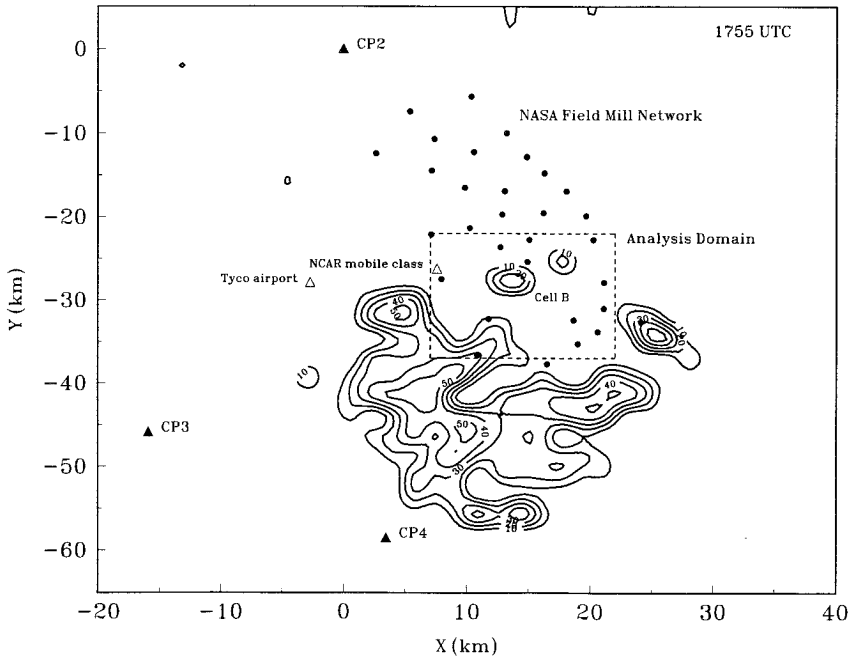

FIG. 2. Location of the NCAR radars CP-2, CP-3, and CP-4 during CaPE. Grid origin is at the CP-2 radar. Dots show locations of the NASA field mill network. The sounding shown in Fig. 1 is a composite of soundings obtained at the two location indicated (Tyco airport, NCAR mobile CLASS). Reflectivity contours are shown at 1755. Contours start at 10 dBZ and increment by 10 dB. Dashed rectangle shows the multiple-Doppler analysis domain.

in a study of convective storms occurring on another day during the CaPE experiment.

By 1803 a number of new cells (marked as A, C, D, and E in Fig. 3b) have formed. Significant w values at 5-km altitude are absent within cell B, which has entered its dissipating phase. The vertical section in Fig. 3b′ cuts through cells E and A. Again positive Z_{DR} columns are nearly coincident with the updraft columns. A few kilometers (~2 km) to the east of cell A, an upper-downdraft region originates near the top (6-km height) and extends downward to the 1.5-km level. Such downdrafts commonly flank the updraft at middle to upper levels in the active growth phase of a convective cell (e.g., Knupp 1987; Yuter and Houze 1995a,b) and provide an effective means of transporting anvil ice to lower levels where natural seeding can occur. It has been speculated that this transport mechanism plays a key role in electrification of thunderstorms (e.g., Vonnegut 1991); however, at this stage of storm evolution none of these new cells show signs of electrification.

At 1808, Fig. 3c indicates strongest updrafts within cell A (peak of 16 m s^{-1} at 5 km) and the adjacent cell D (12 m s^{-1}). The vertical section in Fig. 3c′ shows a positive Z_{DR} column extending to 6.0-km height, with values exceeding 3 dB from 2 to 5 km. Again the upper-level downdraft is visible a few kilometers to the east of the positive Z_{DR} column. Figure 3c also shows superimposed aircraft tracks corresponding to penetration of cell D by the University of Wyoming (WKA) and NCAR King Air (NKA) aircraft. Further details on cell D's internal structure at this time are presented in section 5b.

By 1810 (Fig. 3d) the updraft region of cell A has expanded with peak Z_h and peak w at 5 km being 53.5 dBZ and 13 m s^{-1}, respectively. The dominant cell A

TABLE 2. Radar characteristics of the major cells.

Cell	Max. Z_h (dBZ) at 5.5 km (−6.5°C)	Max. Z_{DR} (dB) at 5.5 km	Max. A_3 (dB km^{-1}) at 5.5 km	Max. height (km) of Z_{DR} = 1.5 dB	Max. w (m s^{-1}) from multiple-Doppler	Height (km) of max. w	Max. height (km) of Z_h = 20 dBZ	Max. IWC (g m^{-3})	Area (km^2) while $w \geq 4$ m s^{-1} at 5.5 km
A	51.6	2.6	1.2	6.6	20	6.3	9.5	3.7	8.8
B	35.5	2.4	0.3	6.0	18	5.8	7.5	1.0	3.6
C	43.0	2.8	0	6.5	15	6.8	9.0	1.8	3.3
D	37.5	1.7	0.2	5.6	12	5.8	7.5	1.4	2.0
E	38.0	1.25	0.3	5.3	13	5.3	9.0	1.9	3.0

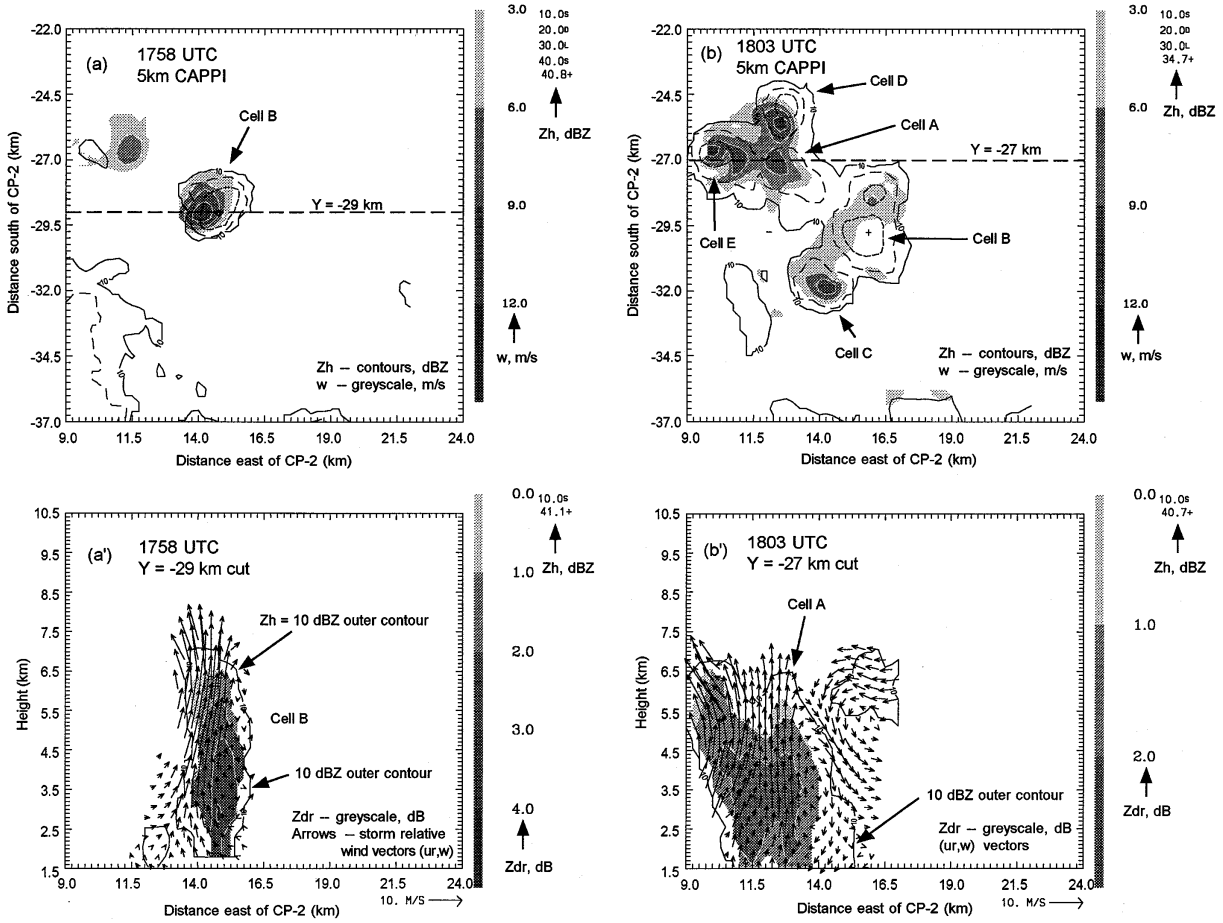

FIG. 3. Constant-altitude (5 km) PPI sections of reflectivity (solid contours starting at 10 dBZ with increment of 10 dB), with gray-scale overlay of updraft greater than 3 m s^{-1} from multiple-Doppler synthesis. Darker shades imply stronger updrafts. Grid origin is at the CP-2 radar. Aircraft penetration tracks are as shown. WKA and NKA stand for the University of Wyoming King Air and NCAR King Air aircraft, respectively. Here, P-3 stands for the NOAA P-3 aircraft, and T-28 indicates the armored T-28 operated by the South Dakota School of Mines and Technology. The times in brackets beside the aircraft name refer to the start of the penetration. The rotated axes (X'', Y'' and X''', Y''') are used later to construct vertical sections of data along the aircraft tracks. CAPPIs are shown at (a) 1758, (b) 1803, (c) 1808, (d) 1810, (e) 1814, (f) 1821, and (g) 1827 UTC. (a′)–(g′) Vertical sections of radar data taken along the Y = constant cut shown in (a)–(g). Cell relative wind vectors (u_r, w) in the plane Y = constant are shown. The Z_{DR} is shown in gray scale with darker shades representing more positive values. The Z_h = 10 dBZ contour outlines the cell boundary. Vertical sections are shown at (a′) 1758, (b′) 1803, (c′) 1808, (d′) 1810, (e′) 1814, (f′) 1821, and (g′) 1827 UTC.

is still in its vigorous growth phase as seen in the vertical section in Fig. 3d′. At upper levels the wind vectors are directed toward the west in response to the southeast ambient winds at and above 7-km height. Figure 3d shows the NOAA P-3 aircraft track penetrating cell A. Rotated X'', Y'' axes are also shown. In section 5a, vertical sections of radar data within the vertical ($Y'' = 0$) plane along the P-3 track are examined in more detail.

Analyzed updrafts within cell A subsided by 1814 (Fig. 3e) at the 5-km level. A new updraft core identified as cell A′ has formed about 2.5 km southeast of cell A. The vertical section in Fig. 3e′ through cell A′ shows a positive Z_{DR} column (again coincident with the updraft column) but only rising to 5.5-km height. The updrafts extend above the Z_{DR} column top from 5.5 km to near the 10-dBZ echo top. The lower height attained by the Z_{DR} column at this time provides support to the hypothesis that ice seeding of the updraft accelerated ice nucleation and growth at lower levels.

At 1821 (Fig. 3f) cell A′ remains dominant, but peak w at 5-km level has decreased from 12 m s^{-1} at 1814 to 8 m s^{-1} at 1821. The vertical section in Fig. 3f′ shows no positive Z_{DR} columns, the 1-dB contour extending only up to 4-km height. The maximum Z_{DR} (in this plane) is only 2.1 dB at 2-km height, suggesting the advanced mature phase of cell A′ has been reached. At 1827 cell A′ begins to show weak downdrafts below 4 km (Fig. 3g′). A fresh updraft center and Z_{DR} column are noted as cell A″ (Fig. 3g) on the southeast side of the complex. Figure 3g shows the T-28 aircraft track penetrating cell A′ and A″ at 1827, as well as rotated

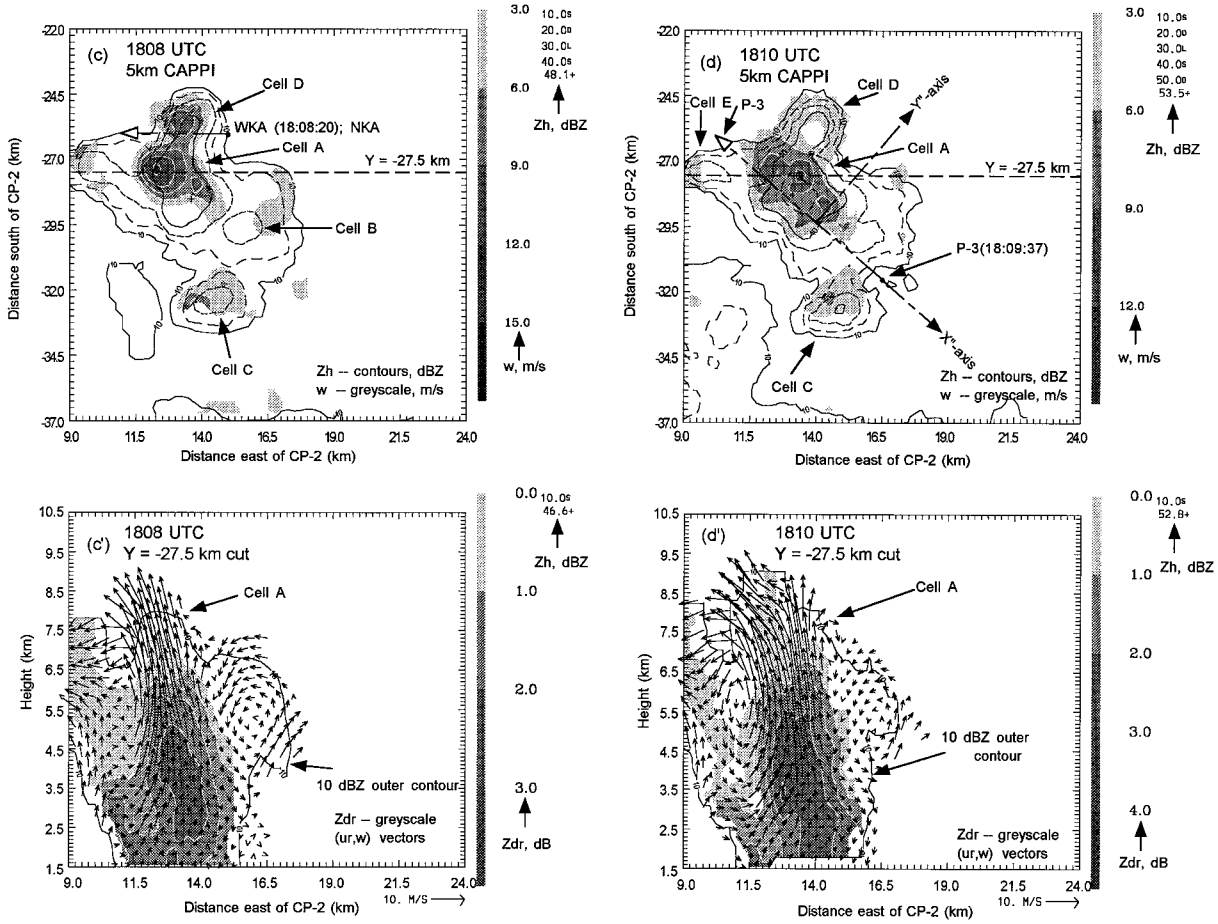

FIG. 3. (*Continued*)

X''', Y''' axes. Further details of cells A′ and A″ are discussed in section 6.

In summary, the multicell storm exhibited a uniform expansion and intensification as individual cells merged and updrafts widened. Precipitation growth was dominated by rain coalescence during the initial vigorous growth stage (through 1810 UTC), after which the ice phase became important. Cell A (and its downshear development cells A′ and A″) were the dominant ones in terms of updraft area, updraft intensity, and reflectivity, and were the only two cells that produced either in-cloud or cloud to ground discharges.

4. Cell characteristics: Early storm development

Cell B, the initial cell of the storm complex (see Figs. 3a,b), formed near 1745 UTC. Its evolution is summarized in Fig. 4 for purposes of comparison with more highly electrified cells considered in the next section. The growth of cell B was rather slow, with the 20-dBZ echo top rising from 3 km shortly after first echo (0 s) to near 8 km after 800 s. Within this time period only one small updraft bubble peaking at 18 m s^{-1} near 400 s (1758) was observed. Positive Z_{DR} columns from ''first echo'' at 1748 and up until 1758 (see also Fig. 3a′) indicate the dominance of warm cloud microphysics during the most vigorous stage of this cell. Significant amounts of ice, as depicted in the IWC field of Fig. 4d, do not appear until after 500 s. Only modest amounts of precipitation (rain mass flux, Fig. 4f) emerge near cloud base about 800 s after first echo.

The NKA detected drops mixed with graupel at 1758 (see Table 1), as well as a strong updraft with peak of 10 m s^{-1}. The corresponding multiple-Doppler-derived updraft (Fig. 3a′) exhibits an overall peak of 18 m s^{-1} near 6.3 km AGL at this time. Weak downdrafts were observed at the cell edges. Cell B dissipated by 1805, with downdrafts detected at 4.0 and 6.5 km by the WKA and P-3, respectively (see also Table 1). No significant electric fields were detected by the NKA or P-3 ($|E_z| <$ 0.5 kV m^{-1}) and no lightning signatures from cell B were found in the surface mill network data.

5. Cell characteristics: Storm vigorous growth period

Since we are interested in relationships among kinematics, microphyics, and electrification, a further anal-

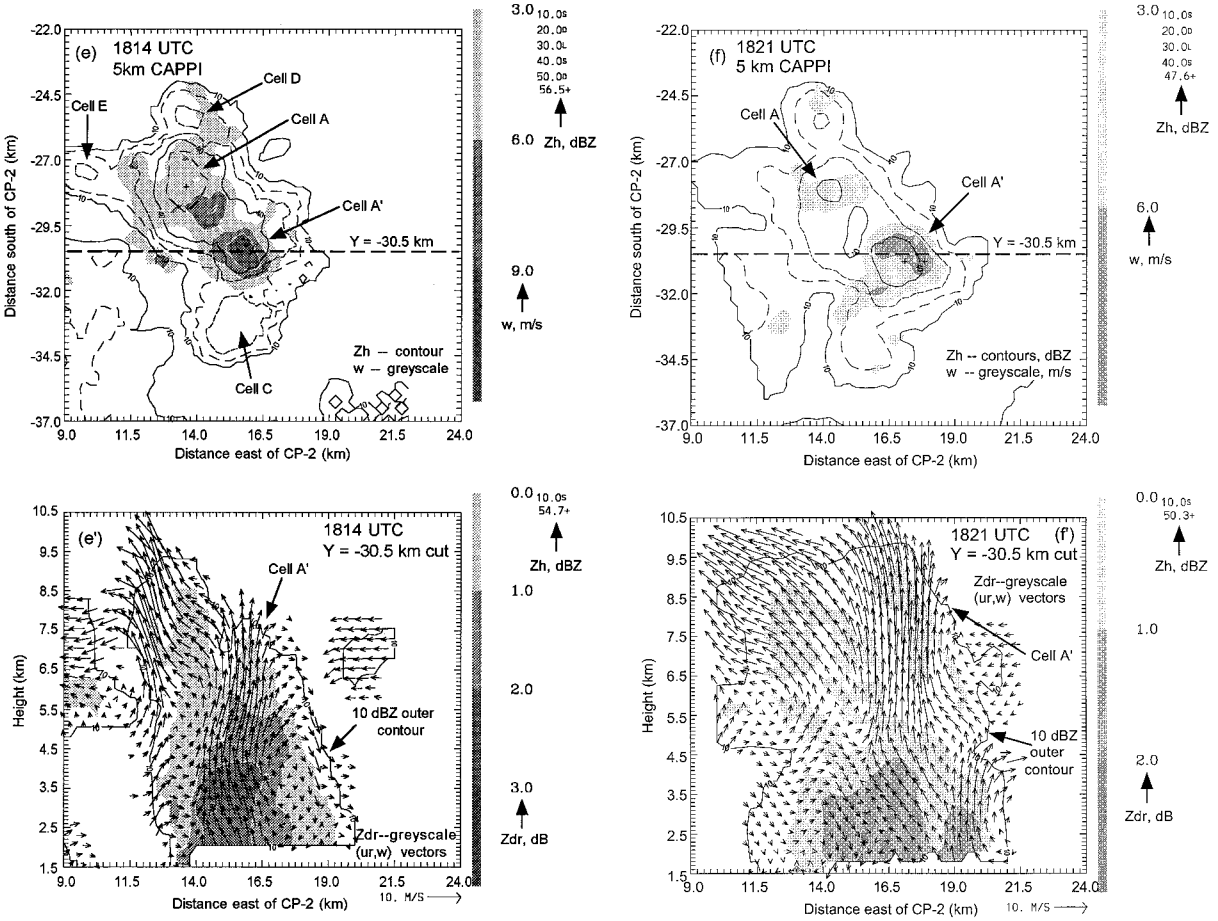

FIG. 3. (*Continued*)

ysis of these coevolving fields is presented focusing on cells A and D. Characteristics of cells A and D are discussed in detail here because of good overlapping coverage in radar and aircraft data. The observed behavior of these cells provides a contrast to that of cell B in that cell D was electrified but produced no discharge, while A was significantly electrified and produced both intracloud and cloud-to-ground discharges. While we treat cells A and D separately for convenience, it is recognized that the component cells interact to varying degrees dynamically, microphysically, and electrically. A future paper will consider the dynamical and microphysical interactions within this storm. Further analysis of the electric field behavior for the early to late mature phases is given in sections 5c (1815 UTC) and 6 (1827 UTC).

a. Cell A

1) EVOLUTION

During the initial vigorous growth phase of the storm (1803–1810), cell A (the second major cell to develop) was dominant and could be easily identified (Figs. 3b–d). During cell A's mature phase (1814, Fig. 3e), cell A′ developed on the downshear side, southeast of cell A. After 1817, the ''box'' was extended to cover cell A′ as well, since A′ was effectively merged with A.

Figures 5a–f show the radar evolution of cell A (followed by A′ after 1817), together with the key aircraft-measured parameters. The vertical bars in Fig. 5b are derived from observations made by the King liquid water probe on the P-3 flying at 6.5-km altitude, which made four penetrations of cell A (or A′ beyond 1817), and the T-28 (Johnson–Williams cloud water meter), which made one penetration at 5-km altitude (see Table 1). The peak aircraft-measured updrafts correlate well in magnitude with the magnitudes derived in the first radar-analyzed *w*-pulse occurring at the times of these penetrations in Fig. 5. A cap of high LDR (≥ -21 dB) values can also be seen in Fig. 5b beginning at 300 s, just as the Z_{DR} contours start to fall.

As cell A evolves, the 1.5-dB Z_{DR} contour descends steadily, the Z_h intensifies below 5 km, and the high LDR cap decreases in height. A second updraft pulse is noted at 700 s (1816) centered aloft at 8-km height (see Fig. 5c); at nearly the same time the main precip-

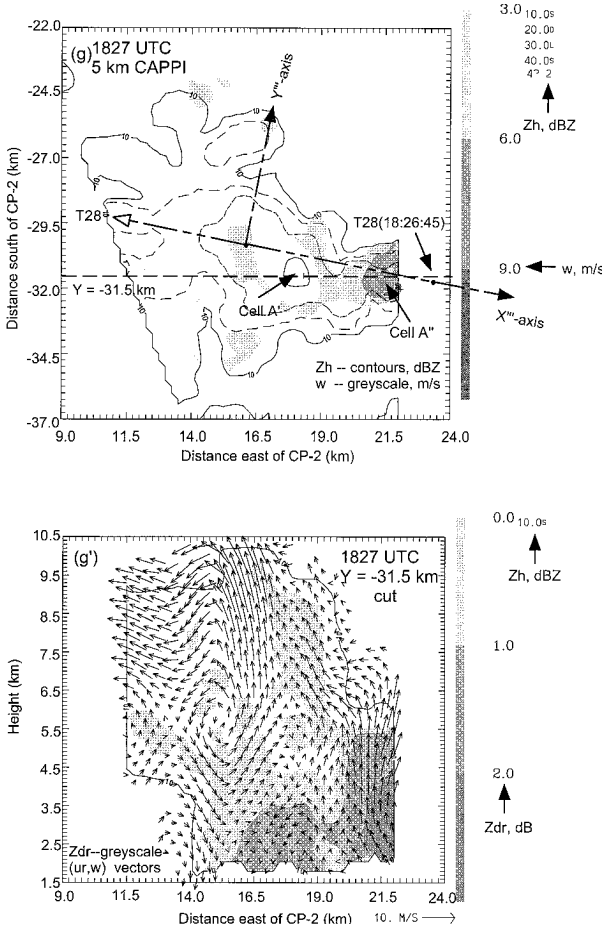

FIG. 3. (*Continued*)

itation shaft is descending with the rain-rate maximum (indicated by A_3 contours in Fig. 5c) at 800 s (1817) at 2.5-km level. The T-28 detects mainly downdrafts near the 5-km level at 1400 s (1827) during portions of its penetrations through cell A′. The P-3 detects updrafts at 6.5 km at 1821 and 1827, corresponding to penetrations through cell A′, which is clearly visible as the third *w*-pulse centered at 8-km altitude at 1200 s in Fig. 5c. As seen in Fig. 5b, these updrafts are associated with moderate cloud water contents (1.5–1.8 g m^{-3}) that are less than the peak values found at the same altitudes in the cell A penetrations at 1805 and 1810.

Radar-derived IWC contours in Fig. 5d reveal a maximum near 4 km (4°C) at 700 s (1816) in response to the first updraft pulse beginning at 300 s (1810). The radar-derived LWC also reaches its peak near 4 km at 700 s (1816). The TIWC profile in Fig. 5f has two local peaks, a relative maximum at 550 s (1813), and the absolute maximum at 800 s (1817). The TIWC peak precedes the rain mass flux peak by approximately 300 s, corresponding approximately to the time required for raindrops to fall from the 0°C height (4.5 km) to the 2-km level.

In Fig. 5d, the slant arrows represent the dipole solutions based on analysis of surface electric field changes due to lightning (Murphy et al. 1996). They represent estimated altitudes and magnitudes of intracloud discharges neutralizing a dipole. The solid dot at the center of each arrow represents the altitude of the dipole center, while the arrow length is proportional to the dipole moment. The arrow points from positive to negative, and the angle from vertical depicts the vertical orientation of the deduced dipole. Note that intracloud (IC) lighting begins around 650 s (1815:30), near the time of maximum IWC (Fig. 5d), LWC (Fig. 5e), and rapidly increasing rain flux at 2 km (Fig. 5f). Dipole moments, centered mainly near 8–9 km, display a tendency to increase with time. The open circles in Fig. 5d are the monopole solutions, interpreted as cloud-to-ground (CG) strokes. Values in brackets are the charge magnitudes neutralized in coulombs. The initial CG flash occurs at approximately 1000 s, about 400 s after the initial IC flash, and 120 s after the peak rain flux at 2-km height.

In Fig. 5e, the arrows represent the maximum vertical component of the electric field from aircraft field mills observed during passages through cells A and A′. The arrows point toward negative charge. An upward-pointing arrow signifies, for example, negative charge above or positive charge below the aircraft level. Further details of the electrical evolution of this cell are discussed in section 5d.

To summarize, the first updraft pulse in cell A at 1810 carries raindrops to low temperatures where they freeze, causing the enhanced LDR cap above (and overlapping with the top of) the positive Z_{DR} column. These frozen drops grow rapidly in the height interval 5–7 km, leading to a maximum rain mass flux (rain rate about 100 mm h^{-1}) at the 2-km level about 600 s after the first updraft pulse. Two upper-level draft pulses of similar magnitude at 1817 and 1824 do not appear to produce any further peaks in the ice or liquid water contents near the surface. The first intracloud discharge occurs at 1815:30, about 6 min after the first updraft pulse above the freezing level and the freezing of raindrops there. Lightning continues until well after the decay of the third updraft pulse.

2) SNAPSHOT OF INTERNAL STRUCTURE AT 1810 UTC

Figure 6 presents data from a P-3 penetration of cell A in the reverse sense of the actual aircraft heading shown in Fig. 3d, that is, from northwest to southeast. The P-3 passes 1 km southeast of the updraft core and resolves two updraft and cloud water maxima with peaks of 12 m s^{-1} and 3.4 g m^{-3} (Figs. 6a and 6b) within the main part of the cell and a small region of weak downdraft on the southeast part of the cell edge marked as XY in Fig. 6a. There is a suggestion of two peaks in the Doppler-synthesized updraft (Fig. 6a), but their lo-

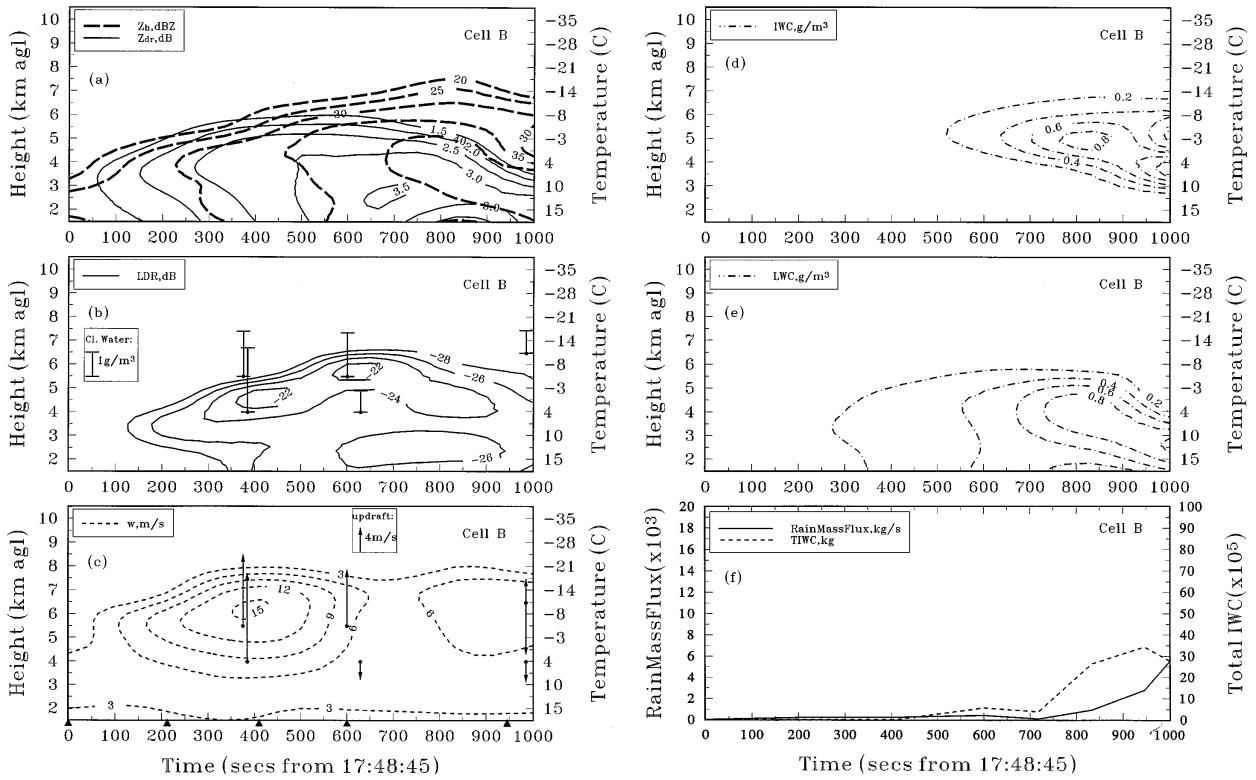

FIG. 4. Time–height contours of radar data for cell B with key aircraft data overlaid. (a) Contours of Z_h (dashed) and Z_{DR} (solid). (b) Contours of LDR with vertical bars representing maximum cloud water detected by aircraft (scale shown in inset box) during penetrations near or through cell B. Solid dot on bottom end of bar shows the penetration altitude. (c) Contours of maximum updraft speed (from multiple-Doppler synthesis) exceeding 5 m s^{-1} (dashed lines). Vertical arrows depict peak updraft–downdraft speeds derived from aircraft during penetrations near or through cell B. Upward (downward) pointing arrows depict peak updraft (peak downdraft) for the penetration with scale shown in inset box. Solid dot depicts aircraft penetration altitude. Solid triangles along the time axis depict times for which multiple-Doppler synthesis were performed. (d) Contours of radar-derived ice water content (IWC). (e) Contours of radar-derived liquid water content (LWC). (f) Time profile of radar-derived rain mass flux (solid) at the 2-km altitude and total ice water content (TIWC, dashed).

cations are offset to the northwest relative to the aircraft observations. Within the updraft region, the Z_h is relatively uniform in the range 40–45 dBZ, with Z_{DR} in the range 1–1.5 dB (Fig. 6c). During this penetration reliable values of enhanced LDR in the range -18 to -20 dB could be detected.

The P-3 2D-P particle imaging probe malfunctioned on this pass. Observations from the 2D-C probe, including reconstructed partial images, show an exponential size distribution for $0.25 \leq D \leq 2.0$ mm (Fig. 6d). The ''flat'' tail extending from 2 to 3.5 mm is probably an artifact due to poor sampling statistics for the larger particles. A superexponential concentration for $D \leq$ 0.25 mm is noted. Other radar parameters along the vertical cut plane along the track are shown in Figs. 6f,g,h. The rotated X'', Y'' axes are marked in Fig. 3d. In Fig. 6f the wind vectors show a broad updraft (peak about 13 m s^{-1}) within the plane of the aircraft penetration. The updraft width ($\sim$4 km) is twice that observed in cell D considered next (section 5b). The 2-dB Z_{DR} contour just reaches up to 6.1-km height. Figure 6g shows contours of Z_{DR} starting at -0.5 dB and increasing in steps of 1 dB, while the LDR values are shown as gray shades with darker shades corresponding to larger LDR. The peak LDR of -17 dB occurs a few hundred meters below the track at 1810:12, within the updraft core.

Between the heights of 5.5 and 6.5 km there is considerable overlap of the positive Z_{DR} column top with enhanced LDR ≥ -21 dB. Figure 6h shows that the peak A_3 of 1.5 dB km^{-1} occurs at 5.7-km height. The positive values extending up to the P-3 penetration altitude indicate the presence of cloud water and liquid–partially liquid particles in sufficient concentrations to attenuate the X-band signal in the range of 0.5–1.5 dB km^{-1} (Vivekanandan et al. 1990; see also appendix A). None of the other cells had such high A_3 values at these altitudes (see Table 2).

This interface region is a mixed phase domain with a mixture of particle types, including liquid drops, frozen, and partially frozen drops (See Figs. 6i–k). The P-3 C-probe with its optical axis vertical should image the circular cross section of liquid drops if there is no airflow distortion of the drops. If the image is elliptical, it is likely that airflow distortion caused it, and by inference, the particle is likely liquid since ice particles

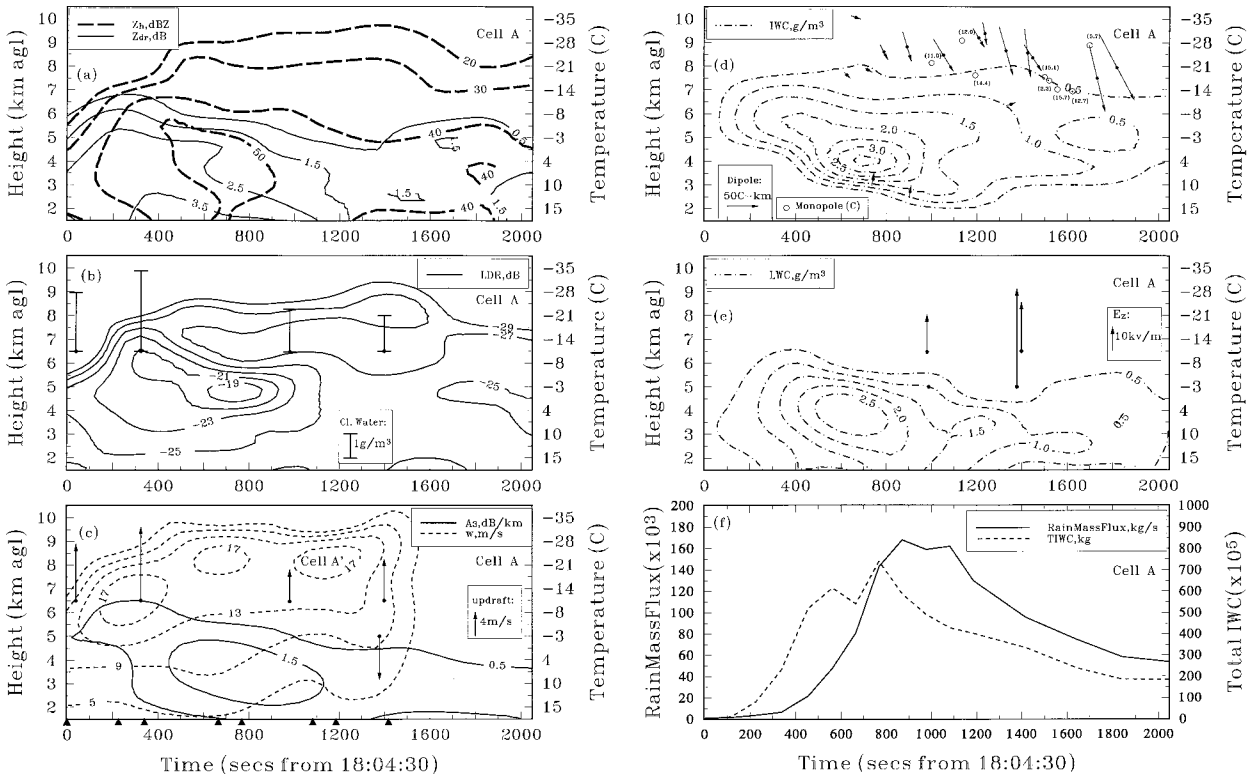

FIG. 5. As in Fig. 4 except for cell A (or later for cell A′). Panel (c) also shows contours of A_3. Slant arrows in panel (d) depict dipole solutions from Murphy et al. (1996). Solid dot at arrow center represents the altitude of the dipole solution, while arrow length depicts dipole moment with scale in inset box. Open circles are monopole solutions with values in brackets being the charge neutralized in coulombs. In panel (e), arrows depict maximum vertical component of electric field from field mills observed during penetration. Arrows point toward negative charge locations. Solid dot represents aircraft altitude.

do not get distorted by the airflow. Thus, if smooth-edged images with elliptical cross sections are seen with the P-3 C-probe, then it is likely that they are liquid. The P-3 C-probe images shown in Fig. 6i span the time sector 1809:53–1809:55, which corresponds to the initial downdraft segment of the penetration near the southeast part of the cell marked XY in Fig. 6a. The images show rough-edged graupel and small ice particles within the weak downdraft. Figure 6j shows images in the sector 1809:57–1809:58, which corresponds to the beginning part of the first updraft pulse encountered. The larger images are now significantly smooth edged, with some elliptical (liquid drops) and some circular (recently frozen drops) shapes, and one with slightly rougher edges indicative of riming. Figure 6k shows images during 1810:12–1810:16, which corresponds to the second updraft pulse encountered. The largest image in Fig. 6k is definitely elliptical in shape, indicating a liquid drop, while the other large ones have smooth edges and with varying shapes from circular to elliptical The more circular ones are likely frozen drops. Thus, this region consists of a mixture of particle phases, which contributes to the large LDR in Fig. 6g at 1810:13, just below the flight path. The enhanced A_3 in the height zone 5.5–6.0 km is a transitory phase of cell evolution; indeed, the overlapping regions of enhanced LDR and A_3 near the top of the positive Z_{DR} column and in the presence of high cloud water (>3 g m^{-3}) indicates a water-rich interface zone where liquid and frozen drops can grow rapidly by collection (Johnson 1987).

Particular emphasis is placed here on interpretation of enhanced LDR and A_3 values found near the top of positive Z_{DR} columns, as these are the first observations of such radar signatures with detailed in situ hydrometeor images. This interface zone is interpreted as a region where supercooled raindrops coexist with partially and fully frozen drops (Smith et al. 1995). Blanchard (1957) has studied the giant ($D \sim 8$ mm) water drops in a vertical wind tunnel. He observed two types of freezing depending on the degree of supercooling attained by the drop at the moment at which freezing begins. The first type is characterized by a clear ice shell forming around the drop. Clear freezing occurs when the wet-bulb temperature T_w is around -5°C. The second type, termed opaque freezing, is characterized by a near instantaneous formation of the opaque or ''milky'' colored ice over the entire surface of the drop and occurs when $T_w < -5$°C. Blanchard also observed that clear freezing drops often remain stable for many

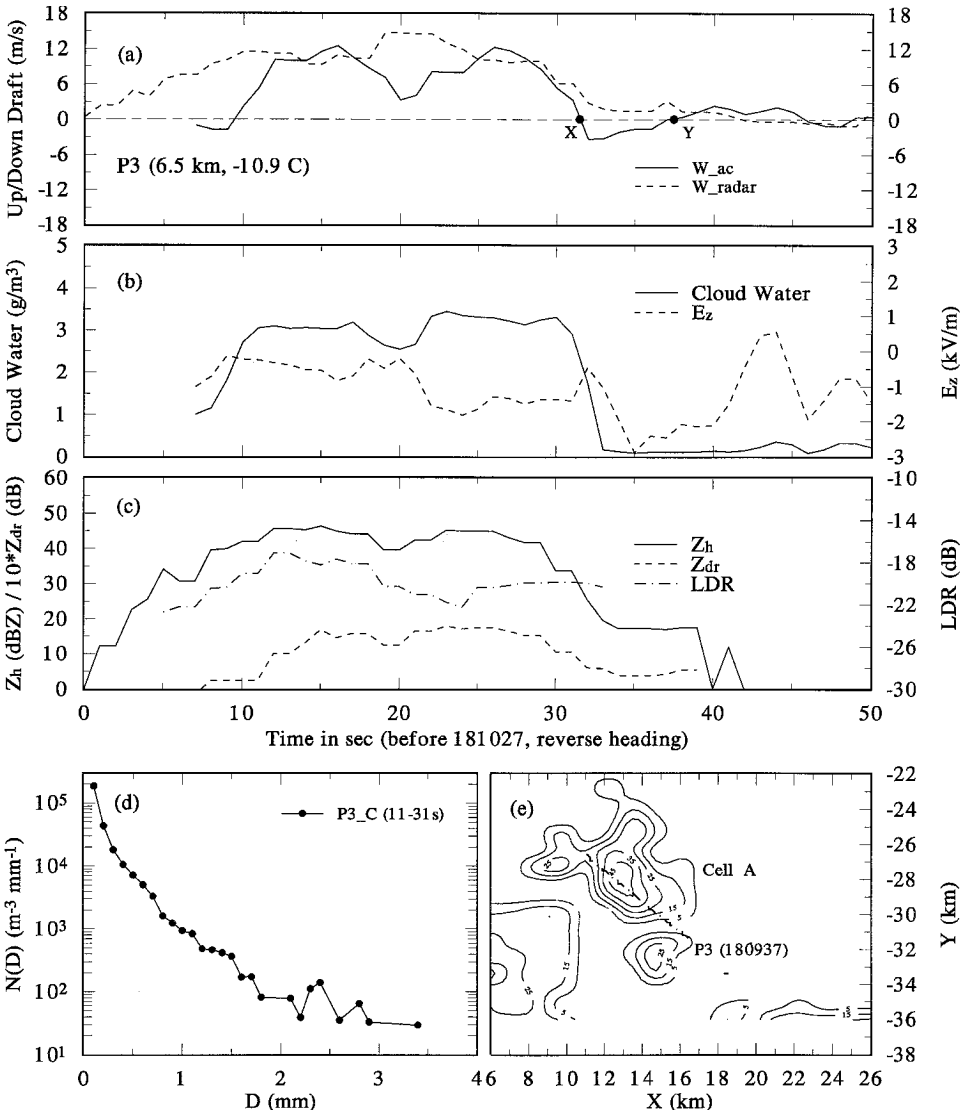

FIG. 6. Multipanel plots of aircraft and radar data corresponding to the P-3 penetration of cell A at 1810 UTC. (a) Vertical winds from aircraft measurements (W_{ac}) compared with multiple-Doppler synthesis (W_{radar} interpolated along the aircraft tracks [see panel (e)]. (b) Cloud water from aircraft probes and vertical electric field component from field mills on the P-3. (c) The Z_h, Z_{DR}, and LDR interpolated along the aircraft tracks. The time axis in panels (a)–(c) is along the reverse of the actual aircraft heading shown in (e). (d) Size distribution from the P-3's 2D cloud probe. (e) CAPPI at altitude of 6.5 km. The P-3 penetration is from southeast to northwest.

minutes, while opaque freezing drops lose orientation stability almost immediately. This loss of stable orientation causes an increase in LDR.

We have used the Mueller matrix–based scattering model (Vivekanandan et al. 1991; Vivekanandan et al. 1993) to compute Z_h, Z_{DR}, and LDR at X-band for an exponential distribution of clear freezing drops. The particles are modeled as oblate water drops (2–8 mm in equivalent diameter with equilibrium axis ratios) with an outer concentric oblate (with same axis ratio) shell of ice of thickness around 1 mm (Bringi and Seliga 1977). The exponential distribution parameters are taken from the 1810 P-3 penetration of cell A during its vigorous growth phase (see Fig. 6d). Using the size distribution data in Fig. 6d, a straight line fit (by eye) is done for $D \geq 2$ mm, resulting in intercept $N_0 = 200$ m^{-3} mm^{-1}, and slope $\Lambda = 1.26$ mm^{-1} (median volume diameter $D_0 = 2.9$ mm). The minimum and maximum equivalent diameters are chosen to be 2 and 8 mm, respectively. The canting angle distribution chosen is the Fisher distribution (Mardia 1972; Hubbert and Bringi 1996), which is equivalent to a two-dimensional Gaussian distribution that has been mapped onto a sphere. This distribution is chosen with mean $\theta = \phi =$

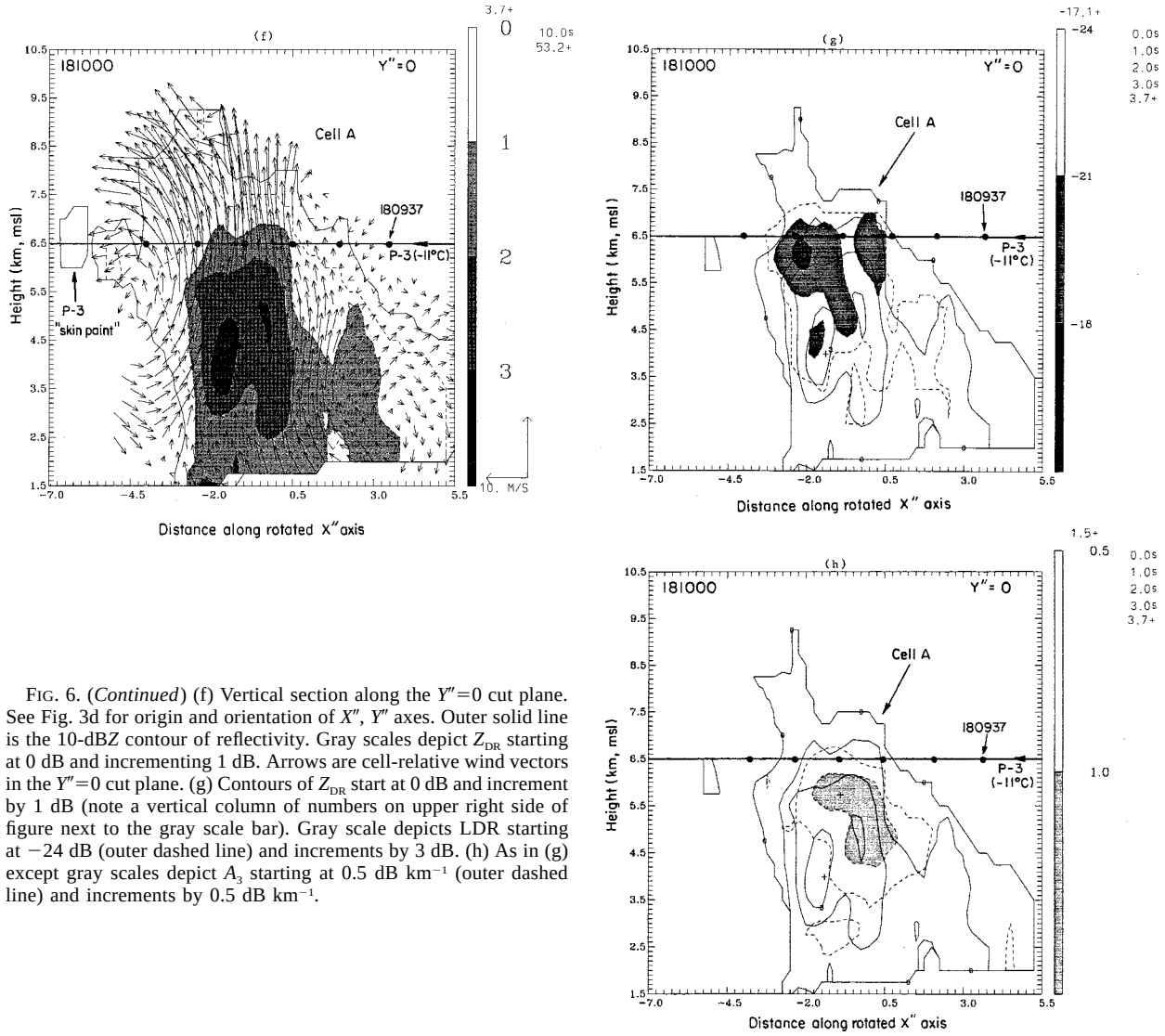

FIG. 6. (*Continued*) (f) Vertical section along the $Y''=0$ cut plane. See Fig. 3d for origin and orientation of X'', Y'' axes. Outer solid line is the 10-dBZ contour of reflectivity. Gray scales depict Z_{DR} starting at 0 dB and incrementing 1 dB. Arrows are cell-relative wind vectors in the $Y''=0$ cut plane. (g) Contours of Z_{DR} start at 0 dB and increment by 1 dB (note a vertical column of numbers on upper right side of figure next to the gray scale bar). Gray scale depicts LDR starting at -24 dB (outer dashed line) and increments by 3 dB. (h) As in (g) except gray scales depict A_3 starting at 0.5 dB km^{-1} (outer dashed line) and increments by 0.5 dB km^{-1}.

0. The equivalent standard deviation (σ) in θ is related to the Fisher distribution parameter κ (Hubbert and Bringi 1996).

Table 3 gives the modeling result for three values of σ. Note that the modeled Z_h agrees well with the radar-measured Z_h of 45 dBZ (see Fig. 6c within the central portion of the penetration). As σ increases, the Z_{DR} decreases and LDR increases as expected. The results for $\sigma = 45°$ are in good agreement with the measured values of $Z_{DR} = 1.5$ dB and LDR $= -20$ dB (Fig. 6c within the uniform Z_h region of the penetration). Thus, the scattering model shows that canted partially freezing drops can give rise to the measured values of Z_{DR} and LDR without invoking wet growth of ice particles (Herzegh and Jameson 1992; Jameson et al. 1996). These are the first computations to show this in a rigorous manner. Even with the high cloud water contents observed during the P-3 penetration (3 g m^{-3}, Fig. 6b), computations show that wet growth is unlikely for particles at -10°C with diameters less than or equal to 7.5 mm. While the largest diameter detected by the P-3 was 3.5 mm, its sampling volume is too small to detect larger drops that likely were present. Since the measured Z_h agrees quite well with calculated Z_h in Table 3 with D_{max} of 8 mm, it appears that wet growth is unlikely given the conditions during the penetration.

b. Cell D characteristics

Cell D was a 2-km-wide bubble-like updraft that formed just to the north of cell A. At mid- to upper levels distinct updraft and Z_h cores were detected, but at lower levels these fields were merged with those of cell A. The evolution of cell D is portrayed in the time–height section (Figs. 7a–f). This cell was penetrated by the WKA and NKA at 1804, 1808, and 1811 and by

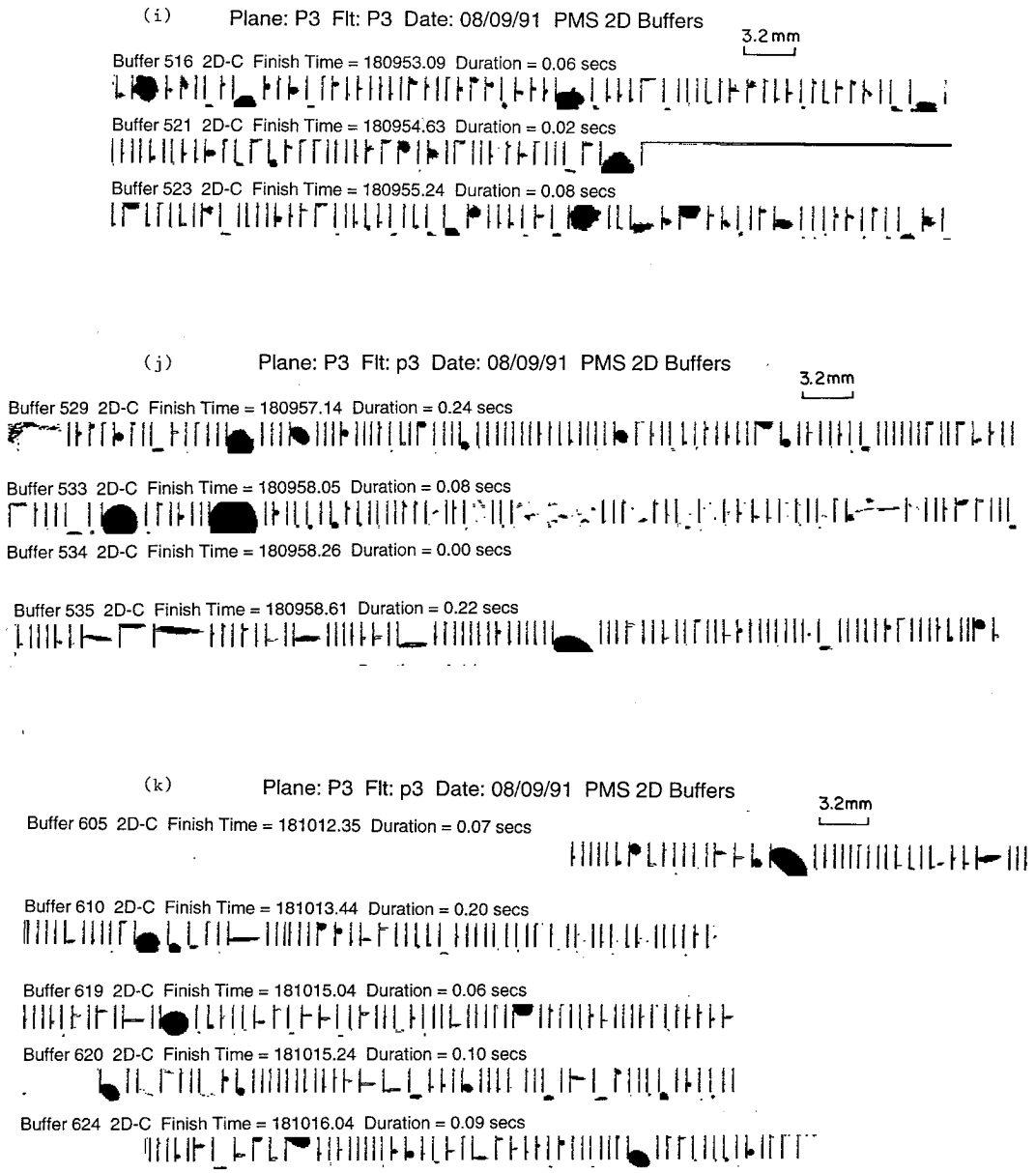

FIG. 6. (*Continued*) The 2D PMS cloud probe images from the P-3. (i) Images from the downdraft region of the penetration from 1809:52 to 1809:55 UTC marked XY in Fig. 6a. (j) Images corresponding to beginning of first updraft pulse from 1809:57. (k) Images corresponding to second encountered updraft pulse from 1810:13 to 1810:16.

three aircraft at 1815 UTC (Figs. 7b,c and Table 1). This good time continuity facilitates an understanding of the coevolving microphysical, kinematic, and electric field evolution within this single-bubble cell, with particular reference to particle size spectra and 2D images during the period 1804–1815.

TABLE 3. Scattering model results.

σ	Z_h (dBZ)	Z_{DR} (dB)	LDR (dB)
20°	44.7	3.5	−20.9
30°	44.5	2.8	−18.6
45°	44.2	1.7	−17.5

Figure 8a shows the particle size spectrum from the WKA's 2D-P probe averaged over the period 1804:25–1804:35 (see also Fig. 7 at 0 s and Table 1) from the cell D penetration at 4-km altitude (2.5°C). As shown in Figs. 7a,c, this penetration was through a 16 m s^{-1} peak updraft accompanied by relatively high Z_{DR} (2.5 dB) and low Z_h (35 dBZ), suggestive of low concentrations of large drops. Large raindrops are implied in the image samples of Fig. 8b. Long streak images are artifacts due to water collecting and then streaming from

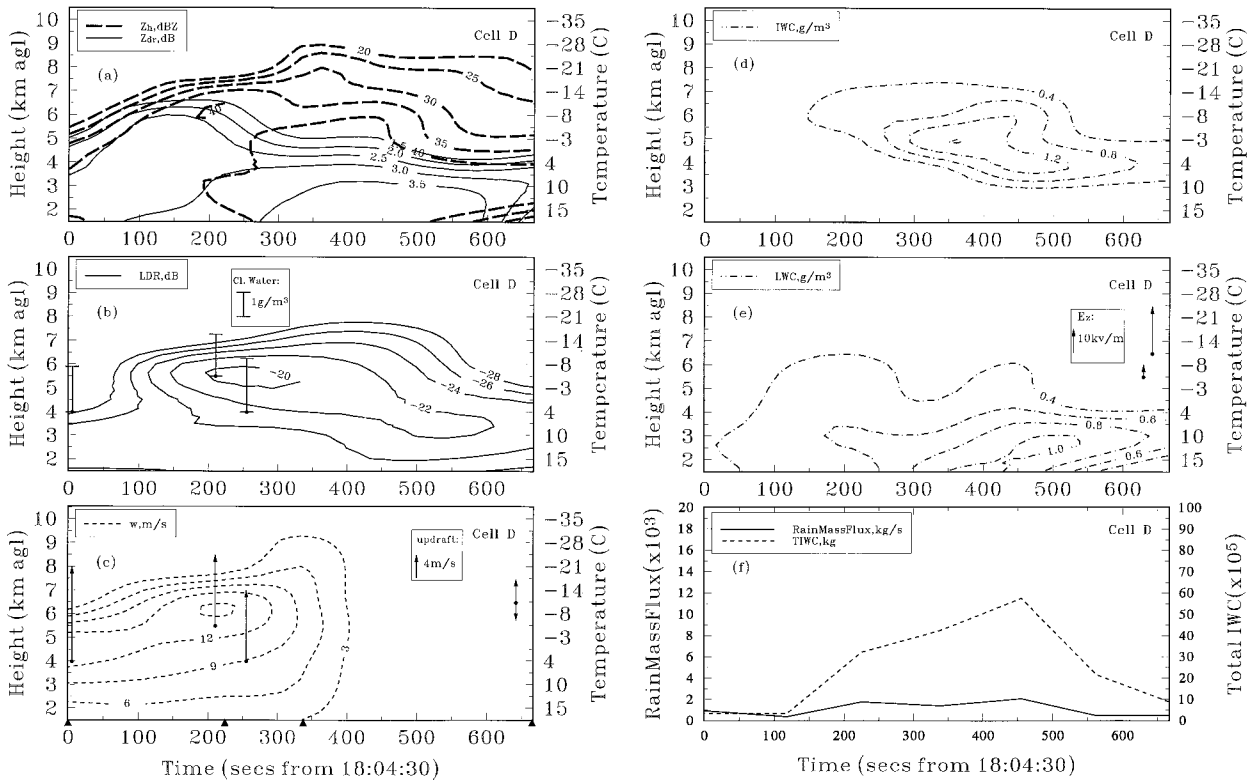

FIG. 7. As in Fig. 5 except data correspond to cell D.

the probe tips through the sample volume. During its penetration through the top of cell D (5.5-km altitude, −6°C), the NKA probes did not detect significant concentrations of particles, cloud water, or E_z at this time.

Detailed measurements are now presented during the vigorous growth phase of cell D at 1808. The strong w pulse in Fig. 7c centered at 6 km at 200 s correlates well with the growth in altitude of positive Z_{DR} between 100 and 200 s in Fig. 7a. As the 1.5-dB Z_{DR} contour starts its downward slope beginning at 250 s, a high

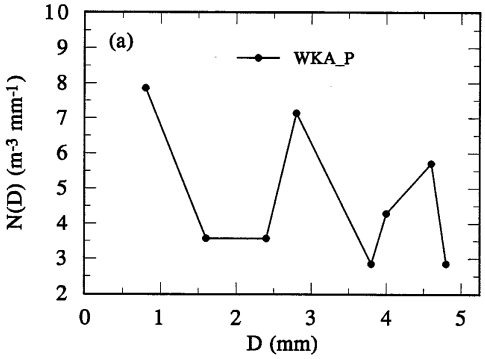

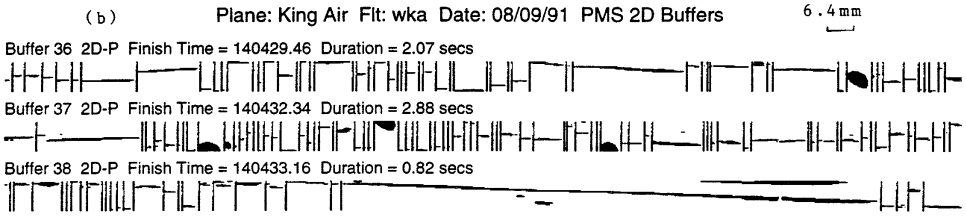

FIG. 8. (a) Particle size spectrum from the Wyoming King Air's (WKA) 2D-precipitation probe averaged over the duration 1804:25–1804:35 UTC corresponding to cell D. Altitude is 4 km (2.5°C). (b) Sample 2D precipitation probe images from WKA at 1804:30. Data are for cell D.

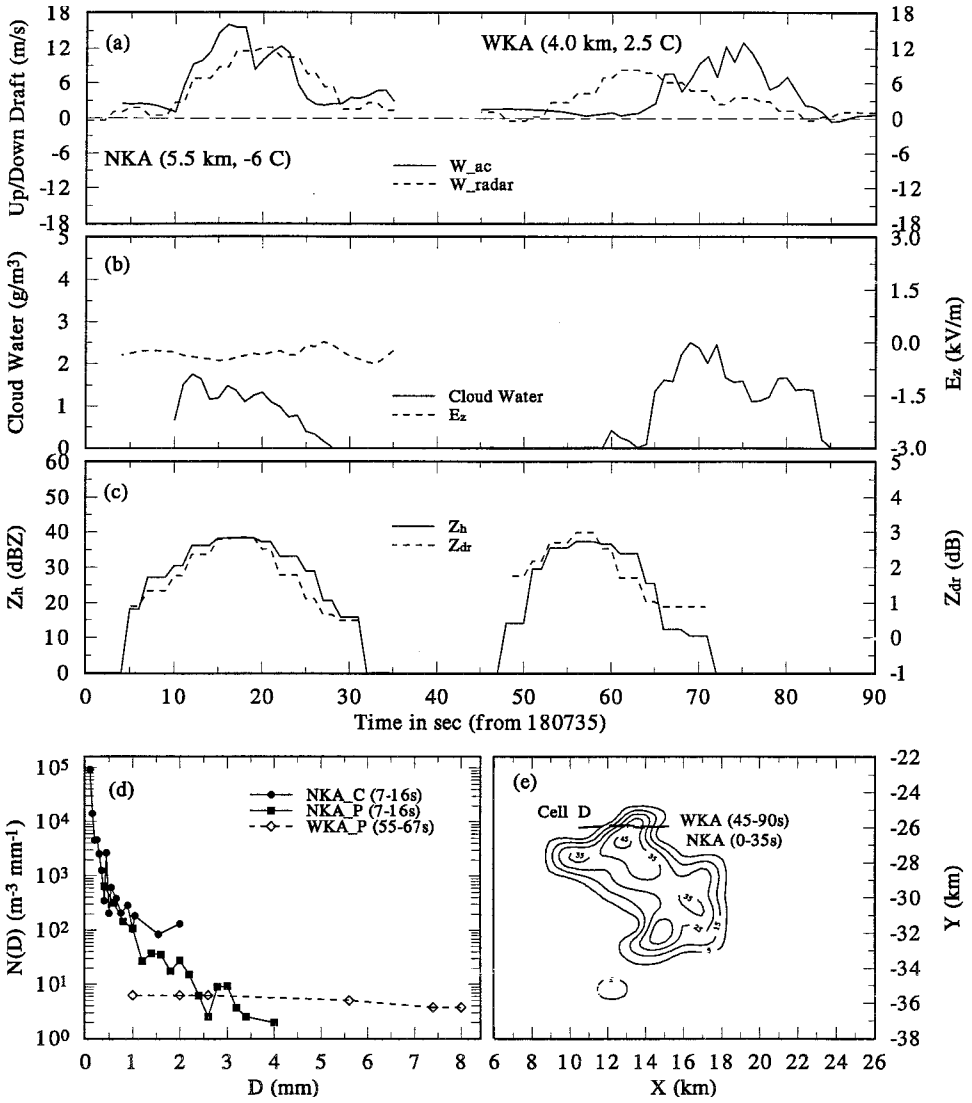

FIG. 9. Multipanel plots of aircraft and radar data corresponding to NKA (immediately followed by WKA along the same heading) penetrations through cell D at 1808 UTC. (a) Vertical winds from aircraft measurements (W_{ac} compared with vertical wind from multiple-Doppler synthesis (W_{radar}) interpolated along the aircraft tracks [shown in panel (e)]. (b) Cloud water from aircraft probes (solid line) and vertical electric field component (dashed) from field mills on NCAR King Air (NKA). (c) The Z_h and Z_{DR} interpolated along the aircraft tracks. (d) Particle size distribution from aircraft PMS probes (C—cloud probe, P—precipitation probe). (e) The Z_h contours starting at 5 dBZ with increments of 10 dB. CAPPI altitude at 5.5 km. Thick and long dashed line depicts NKA and WKA tracks, with WKA's penetration 40 s behind NKA along the same track (see also Fig. 3c).

LDR cap forms near 6 km (Fig. 7b). About 100 s later, the peak IWC (1.5 g m^{-3}) is estimated at 4.5-km height near the melting level (Fig. 7d). Care must be exercised in interpretation of large LDR values in the presence of strong Z_h gradients (up to 20 dB km^{-1}) within small cells (2–3-km diameter) such as cell D. Simulations show that antenna pattern effects can bias LDR quite high, and thus the LDR cap alluded to earlier may be an artifact. This does not apply to cell A whose diameter was significantly larger and Z_h gradients less severe.

Aircraft penetration data through cell D at 1808, about 5 min after first echo, are presented in Fig. 9. The two King Airs flew vertically stacked coordinated penetrations near this time at the 4- and 5.5-km altitudes with NKA in the lead (see Fig. 3c). The WKA measured a peak updraft of 12 m s^{-1}, higher than w_{radar} at its level, with w_{radar} displaced about 1 km away east of w_{ac}. Figure 9b shows peak cloud water contents of 1.75 g m^{-3} from the NKA and 2 g m^{-3} from the WKA. Figure 9c depicts Z_h and Z_{DR} along the track. The Z_h peaks around 37 dBZ with Z_{DR} peaks of around 2.7 dB at both levels. This combination of relatively low Z_h and moderate to large Z_{DR} is

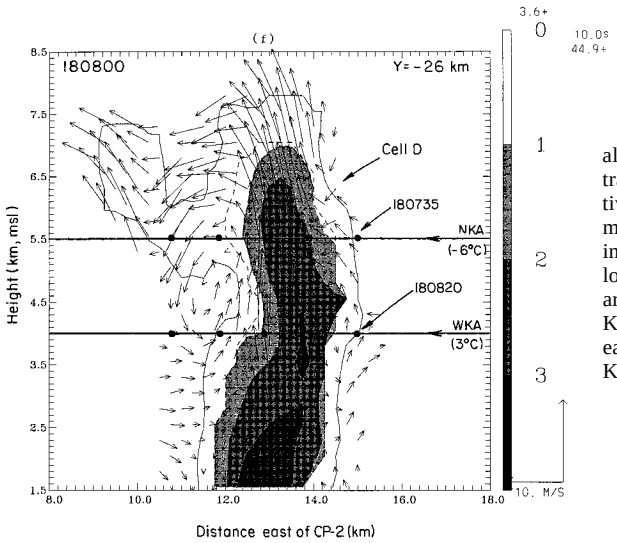

FIG. 9. (*Continued*) (f) Vertical section of radar data along the $Y = -26$ km cut plane, i.e., along the aircraft track. Outer solid line is the 10-dBZ contour of reflectivity. Grayscales depict Z_{DR} starting at 0 dB and incrementing by 1 dB. Arrows are cell-relative wind vectors in the $Y = -26$ km cut plane with scales shown on the lower right corner of the panel. NKA and WKA tracks are shown with solid dots separated by 10 s. (g) NCAR King Air 2D-P probe images at 1407:50 (note this is eastern daylight time, add 4 h for UTC). (h) Wyoming King Air 2D-P probe images (note eastern daylight time).

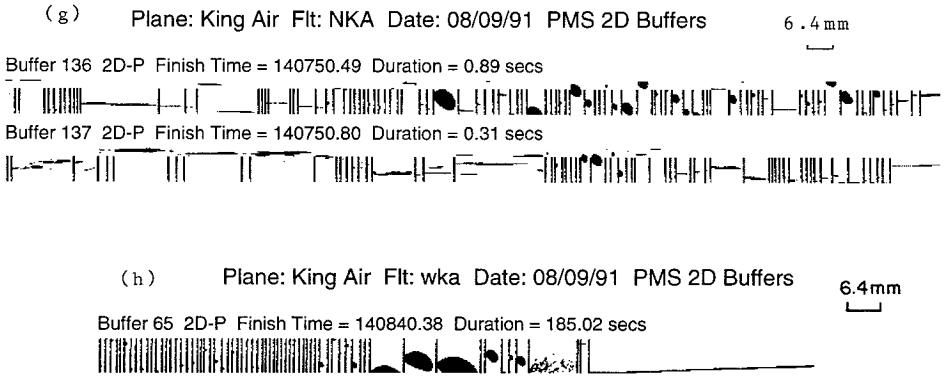

common in the vigorous growth phase of warm-based clouds (Illingworth et al. 1987; Bringi et al. 1991), but the observations reported here are the first verification of these signatures using penetrating aircraft.

Figure 9f shows a vertical section of radar fields along the flight path ($Y = -26$ km in Fig. 9e), which portrays a vertically erect positive Z_{DR} column with the 1.5-dB contour rising to 6.7 km (-12°C). This column is centered on the updraft column; both fields are about 2 km wide. The maximum Z_{DR} within the column is found at 1.8-km altitude, well below the aircraft penetration levels, which provides evidence of large drop sorting as discussed below.

Figure 9d presents raindrop size spectra from 2D-PMS probes on the two aircraft. The NKA was equipped with both 2D-C and 2D-P probes, while the WKA was equipped with a 2D-P. The WKA detects only a few large drops ($D \sim 6$–8 mm), whose images are shown in Fig. 9h. At this level w_{radar} peaks at 9 m s^{-1}, with most values around 6 m s^{-1}. Thus, the large drops are actually descending through this level and growing further by collection in the presence of abundant cloud water, leading to the drop-sorting effect alluded to above (Bringi et al. 1991). At the NKA level, the exponential size spectrum for $D > 1$ mm (Fig. 9d), with a super-exponential concentration of smaller particles, is in sharp contrast to the WKA distribution, even though the Z_h and Z_{DR} are nearly the same at both levels. Clearly the 2D-P-derived size spectrum from the WKA is not representative of the true concentrations of drops in the updraft at the WKA level. Some NKA 2D-P images are shown in Fig. 9g. They are all drops with one big drop ($D \sim 4$ mm) detected. It is likely, given the updraft magnitudes at this level (~ 12 m s^{-1}), that all drops detected at the NKA level must have ascended through this level from below.

The above observations show that warm rain processes were dominant within the positive Z_{DR} column at 1808 UTC. The presence of very large drops (to 8 mm) in the presence of very low concentrations of small drops at 4 km implies a very active coalescence process extending to relatively high levels. These measurements are similar to those described by Rauber et al. (1991) for much shallower convective clouds. No evidence of ice particles (rough-edged images) was found in the 2D-C or 2D-P images at the NKA flight level, though partially frozen drops cannot be excluded.

The 1811 UTC penetration (see also rows 3a, b under

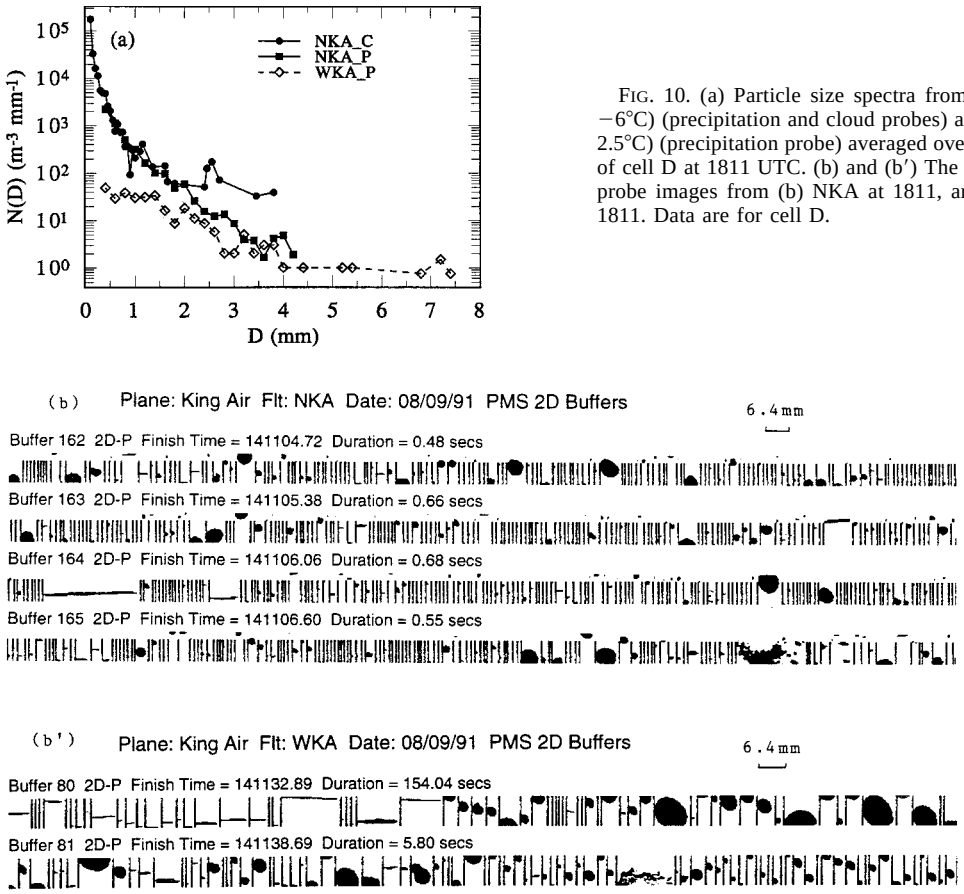

FIG. 10. (a) Particle size spectra from NKA (5.5 km, −6°C) (precipitation and cloud probes) and WKA (4 km, 2.5°C) (precipitation probe) averaged over the penetration of cell D at 1811 UTC. (b) and (b′) The 2D precipitation probe images from (b) NKA at 1811, and (b′) WKA at 1811. Data are for cell D.

cell D in Table 1), summarized in Fig. 10, shows the size spectra from the 2D probes (Fig. 10a) and sample images from the NKA's 2D-P probe (Fig. 10b, top panel) and the WKA's 2D-P probe (Fig. 10b′ bottom panel). The NKA images from the −6°C level are smooth but not elliptical in cross section (as in Fig. 9g), indicative perhaps of recently frozen drops. Similarly, the WKA images from the 2.5°C level are smooth (and much larger) but not as elliptical as in Fig. 9h, indicative perhaps of slightly melted ice particles with an inner frozen drop core. We note in Table 1 and Fig. 7c that the updraft had substantially weakened by 1811 (after the vigorous pulse at 1808) and the positive Z_{DR} column had subsided (Fig. 7a) relative to its extent at 1808. The NKA did not detect measurable (>1 kV m^{-1}) electric fields on this pass.

Figure 11 shows similar data from the 1815 penetrations of cell D (see also Table 1) by the NKA and the P-3 (slightly to the southwest of the center of cell D). The cell collapsed by 1815 (660 s) as indicated by P-3 measurements of weak up- and downdrafts at 6.5-km height and weak updraft in the multiple Doppler analysis (Table 1 and Fig. 4). Because cell D tilts to the northwest in response to the shear, the P-3 actually penetrates the upper part of cell D at 6.5 km (−11°C). The size spectra from both the NKA and P-3 in Fig. 11a are similar for $D \leq$ 1.5 mm. The images in Fig. 11b (from the NKA's 2D-C probe where times are in local time, that is, UTC − 4 h) are all indicative of rough-edged graupel similar to images from the P-3's 2D-C probe (Fig. 11b′). Although only weak up- and downdrafts were detected (Table 2), higher values of vertical electric fields were measured (5 kV m^{-1} from NKA and 20 kV m^{-1} from P-3), indicating negative charge above the P-3's flight level. The sequence of particle images shown in Figs. 9g, 10b, and 11b clearly illustrates the transition in hydrometeor type (at the −6.5°C level of the NKA) from raindrops at 1808, to frozen drops (perhaps increasing in size via riming yet with smooth surface) at 1811, to a uniform mixture of ice crystals and rough-edged graupel at 1815. These observations are consistent with an electrification process that is more effective when graupel with "dry" and rough surfaces is more abundant and when the midcloud region contains a mixture of updrafts and downdrafts.

c. Further analysis of electric field observations during the vigorous growth phase

Initial electrification of cell A was noted during the P-3 penetration at 1809 (Fig. 6b). Near 1815, four instrumented aircraft, that is, WKA, NKA, T-28, and P-3 pen-

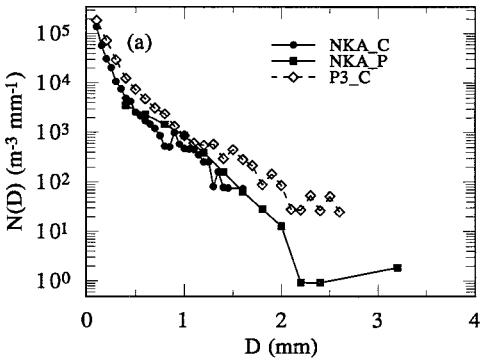

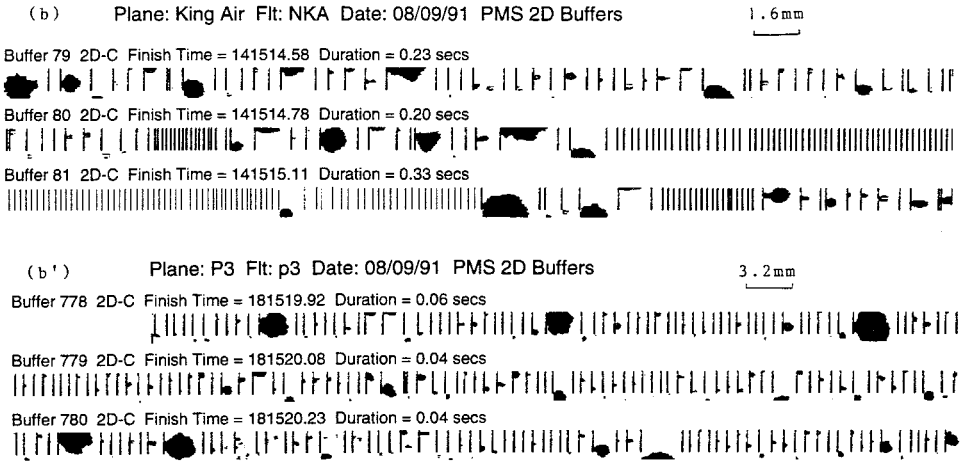

FIG. 11. (a) Particle size spectra from NKA (5.5 km, −6°C) and P-3 (6.5 km, −11°C) at 1815 UTC corresponding to cell D. (b) and (b′) The 2D cloud probe images from (b) NKA at 1815, and (b′) P-3 at 1815. Data are for cell D.

etrated or passed near cells D, A, and A′. Figure 12 shows a 5.5-km CAPPI (constant-altitude plan position indicator) at 1815 with NKA, P-3, and T-28 tracks superimposed. Relative locations of updrafts are shown in Fig. 3e. Arrows perpendicular to the tracks in Fig. 12 depict the horizontal electric field component locally perpendicular to the track, while one- and two-digit numbers plotted along the track identify local extrema of the vertical electric field component. The positive direction is away from positive charge and toward negative charge. Uncertainty in the measured component along the track prevents depiction of a true three-dimensional electric field vector. The NKA (near 5.5 km) and T-28 (near 5.1 km) are moving from right to left (westward), while the P-3 (near 6.5 km) is moving from upper left to lower right (southeastward).

All three aircraft pass along the northeastern edge of the main echo associated with cell A and near or through the remnants of cell D. The central region of cell A appears to have negative charge associated with it in the 5.1–6.5-km altitude region, based on the transverse electric field components pointing in its direction from all three aircraft. Weak positive vertical field components (<5 kV m^{-1}) determined by the P-3, which approaches cell A most closely, suggest that this charge is centered above the P-3 (6.5 km). The P-3 also detected another charge center associated with cell A′ based again on the transverse electric field components it sensed just after 1816.

The P-3 and NKA pass in opposite directions on opposite sides of the remnants of cell D, whose midlevel updrafts had dissipated approximately 400 s earlier. The transverse field components from the two aircraft point inward toward the center of cell D, suggesting a negative charge center. Positive vertical components from both sides, and a stronger positive component (20 kV m^{-1}) determined by the P-3, which passes closer to the center, suggest that the negative center is not too far above the P-3 altitude (6.5 km).

The P-3 measured a weak negative vertical field component and strong northeastward-directed transverse component as it approached cell D in the clear from the northwest. This may be due to positive charge in the anvil streaming northwestward from this end of the storm, centered some distance southwestward of the P-3 track.

The T-28 detected another probable midlevel negative charge center associated with an updraft region detected by it, but not by multiple-Doppler analysis, as it left the storm moving westward from the main echo at 1816:30. This is a new convective region developing to the northwest of cell A.

Particle charge data from the P-3 are shown in Fig.

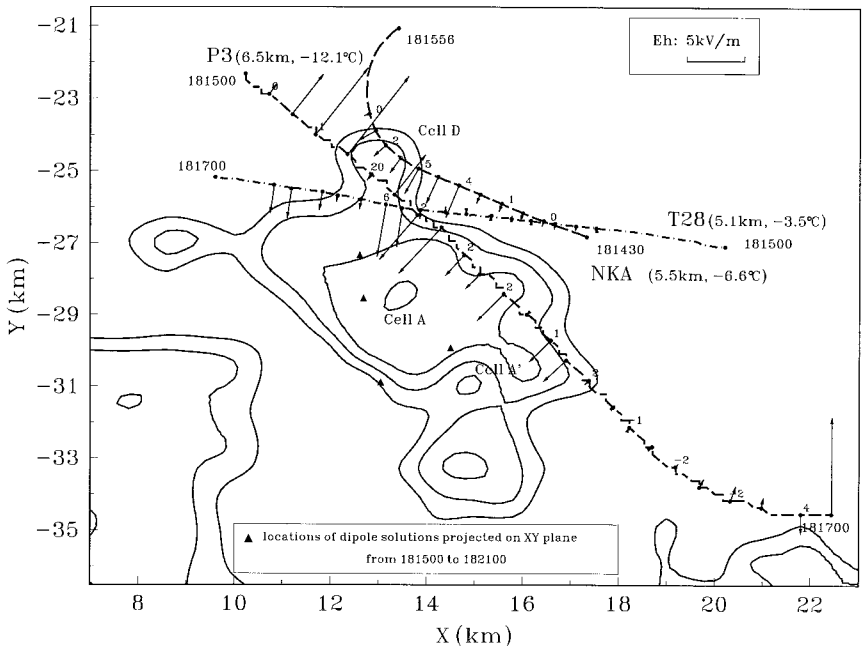

FIG. 12. Constant-altitude (5.5 km) PPI section at 1815 UTC with Z_h contours (solid lines) starting at 10 dBZ and incrementing by 10 dB. The T-28 (5.1 km MSL), NKA (5.5 km), and P-3 (6.5 km) penetration tracks are shown. Arrows perpendicular to the track at 5-s intervals depict the horizontal electric field component (E_h) locally perpendicular to the track (scale given in the inset box). One or two digit numbers along the track identify the magnitude of the local vertically directed electric field component (E_z). Arrows point away from positive charge, and a positive vertical component indicates negative charge above or positive below. Times are indicated at the ends of each track.

13a, with net charge shown in Fig. 13b (data from Brooks 1993). Observations are intermittent in updraft regions due to signal corruption from cloud water shedding from the induction ring used to detect particle charges. Outside of updraft regions, particles of both sign are detected, with a tendency for negative charge to dominate in the cell D region. Although these charges were found in regions of precipitation, the identity of the charge carriers is not known. The concentration of charged particles ($Q > 45$ pC) detected is much less than 1% of the total precipitation particle concentration and an even tinier fraction of the total cloud particle concentration.

Murphy et al. (1996) could resolve less than one-half of the lightning events associated with this storm into monopoles or dipoles. The locations of the solutions that they were able to obtain for events occurring between 1815 and 1821 (projected onto the X–Y plane) are also shown in Fig. 12. These same events are also depicted in time–height format in Fig. 5d.

At 1815, lightning is just beginning in this storm (Fig. 5d at 600 s), which is when the NKA left the storm complex. All resolvable events until 1819:30 are intracloud and all lightning for the entire storm lifetime is associated with cells A and A′. All but two of the intracloud lightning events prior to 1819:30 are consistent with a positive charge layer near storm top and a negative layer in the 7–8-km region. There are two weak upward-pointing dipole solutions well below the freezing level near 720 s (1816:30) and 900 s (1819:30), which, if correct, do not fit well with the traditional picture of thunderstorm electrification being initiated by collisions between ice particles well above the freezing level.

6. Mature stage structure at 1827 UTC

a. Radar and aircraft observations

As an example of aircraft penetrations through a mature cell, we consider cell A′. Figure 3g indicates that the T-28 passed through the updraft–reflectivity core region near 1827. Cell A to the northwest had weakened considerably by this time. However, a new updraft center is located as cell A″ in Fig. 3g, southeast of cell A′.

Figures 14a–c show the T-28 data plotted along its reverse heading so that data are progressing in a northwest–southeast direction. An updraft/cloud water pulse (80–110 s) was encountered along the southeast edge in a region where a new convective cell (A″) is developing (marked as AB in Fig. 14a), while the south flank of the main cell (A′) shows downdrafts up to -6 m s^{-1}. The vertical section of radar-derived vertical winds and Z_{DR} along the T-28 track (Fig. 14f, identified as X''' axis)

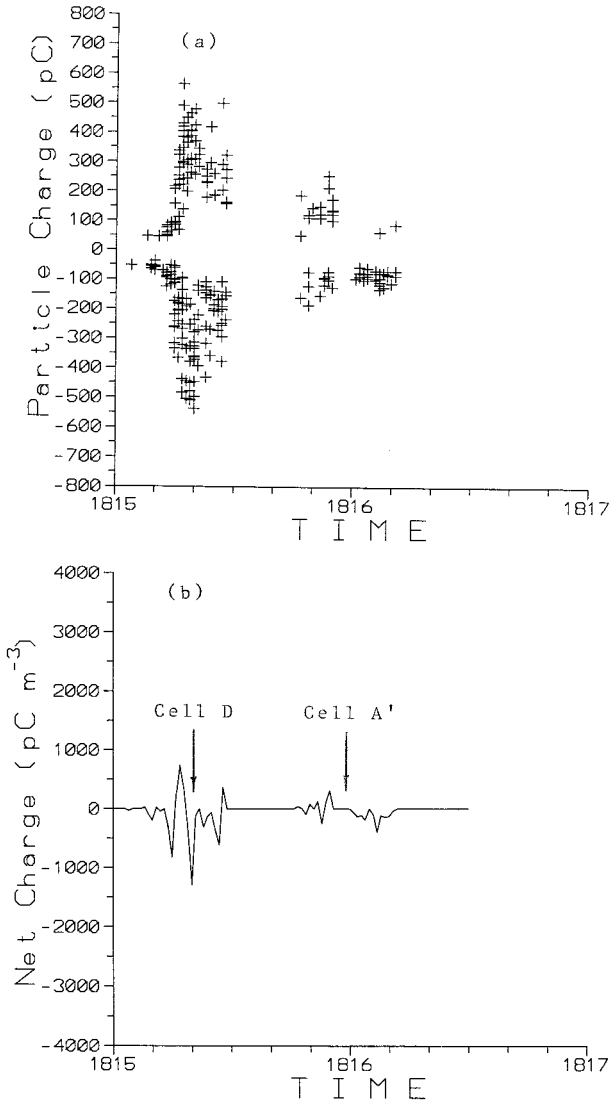

FIG. 13. Particle charges deduced from induction ring device on P-3 (from Brooks 1993) along track shown in Fig. 12 from 1815:00 to 1816:30 UTC. (a) Individual particle charges. (b) Net charge. Altitude of P-3 is 6.5 km.

reveals a positive Z_{DR} column (cell A″) extending to 5.5 km on the southeast (downshear) edge of cell A′, centered on the updraft column marked as AB in Fig. 14a. The broad updraft at mid- to upper levels with the wind direction turning to the northwest aloft represents the main core of cell A′. Weak downdraft areas are located below 5 km within the Z_h core. There is no positive Z_{DR} column within cell A′ and no enhanced LDR values (≥ -21 dB) are found anywhere (Fig. 14c). The Z_{DR} structure below the melting level in this region is more characteristic of melting ice forming raindrops, characteristic of the late mature stage of a thunderstorm cell.

Figure 14g shows T-28 2D-P probe images within the cell A″ marked as AB in Fig. 14a, which indicate liquid drops, and streak images from shedding cloud and rainwater. The presence of raindrops was confirmed by the T-28 Cannon particle camera photographs (not shown here). The T-28's 2D-P probe was oriented with horizontal optical axis, and with no flow distortion it should depict the drop's elliptical cross section. Note that the time on the T-28 images is in eastern daylight time (add 4 h to get UTC).

The T-28 2D-P probe images (Fig. 14g) from the central part of cell A′ (1827:50–1827:53) indicate rough-edged graupel. The corresponding size spectra are in Fig. 14d. The T-28 (44–73 s) spectrum, acquired from the central region of the cell A′, is dominated by graupel particles. Low LDR values (-27 dB) and near-zero Z_{DR} imply low-density particles in this region. The other T-28 (85–119 s) spectrum is from cell A″ indicates a lower concentration of liquid drops, up to 3 mm in diameter with an exponential distribution. Reliable LDR measurements are difficult in this region because of the high Z_h gradient on the southeast edge of cell A″. This causes LDR to be biased high to -24 dB.

The aircraft information at this time reveals the dramatic contrast between the young developing cell A″ on the southeast side of the storm and the more mature cell A′ nearer the central region of the storm. Within cell A′ the updraft has decayed at mid- and lower levels, graupel is the predominant form of precipitation above the freezing level, and electrification is evident. Within the newer cell A″, only rain, frozen raindrops, and cloud water are present in the updraft just above the freezing level and the updraft maximum is still centered at low to midlevels.

b. Electric field observations from aircraft penetrations

The T-28 and P-3 coordinated on two more penetrations of cell A′ (after the King Airs departed) at 1821 (see row 3 in Table 1) and at 1827 (rows 4, 5 in Table 1, also Fig. 3g). We discuss here electric field observations in the mature phase from the last coordinated penetration at 1827 (Fig. 15) presented in the same format as in Fig. 12. The charge distribution is more complex as the storm system evolves and lightning is added to the list of processes acting to redistribute charge in the cloud.

The most active convection at this time is penetrated by the T-28 as it enters from the east (see also Fig. 3g). The generally positive vertical field components from both aircraft are consistent with negative charge above and/or positive charge below both aircraft through most of the storm. Along the P-3 track, on the northwest side of the storm, negative E_z is probably due to positive charge in the anvil overhead.

The transverse components measured along the two tracks switch sign several times, suggesting multiple discrete charge centers in the storm. There is a dramatic shift in sign near the west end of cell A′ ($X = 17$, $Y = -30$). The interpretation of the locations of these charge centers would depend on whether they were assumed to be pos-

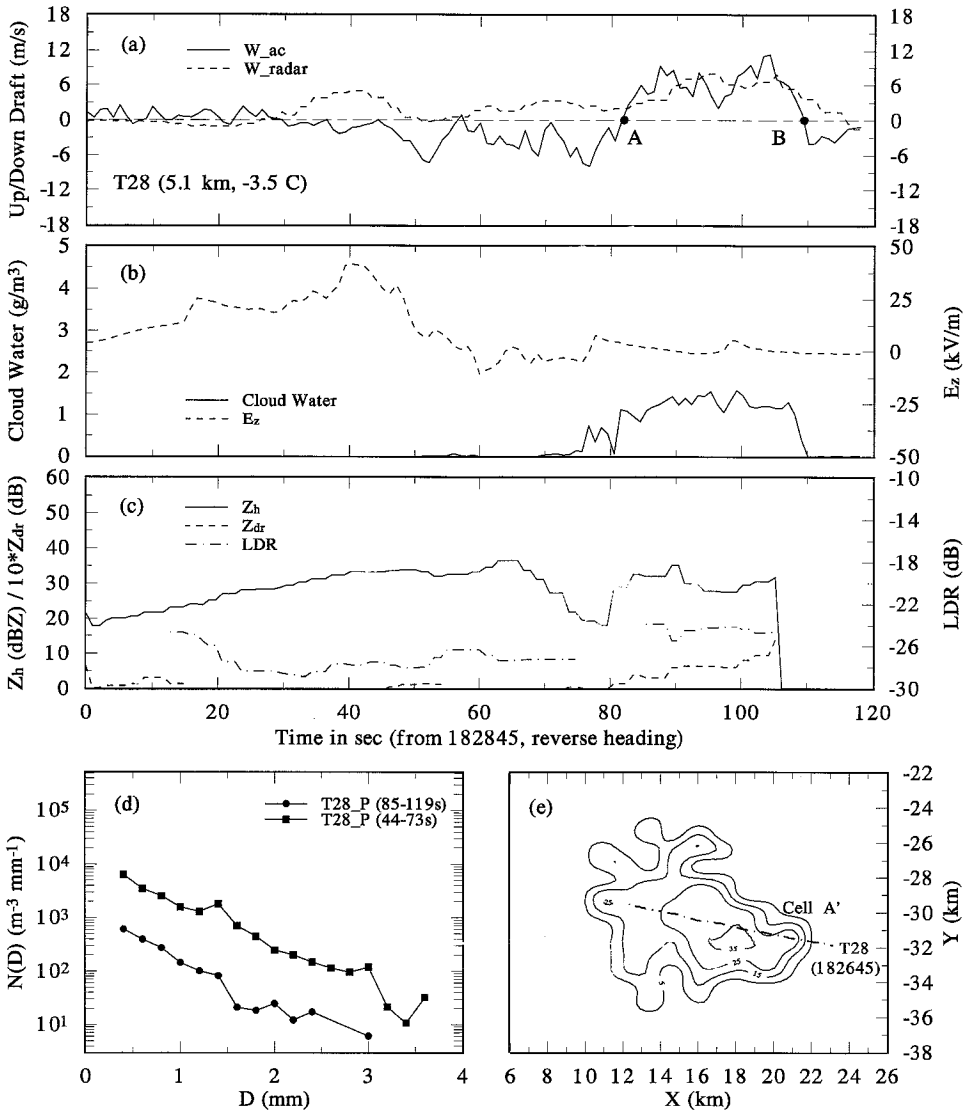

FIG. 14.(a)–(c) As in Fig. 6 except panels (a)–(c) correspond to the T-28 penetration. Note, time axes in panels (a)–(c) are along the T-28's reverse heading. Sector AB in panel (a) refers to the new updraft region southeast of cell A′ marked as A″ in panel (f). (d) As in Fig. 6d except size distribution data shown from the T-28's 2D precipitation probe for two sections of the penetration. (e) As in Fig. 6e except CAPPI at 5.1-km altitude.

itive charge below or negative charge above the aircraft levels, or some combination thereof. The coordinated switch in direction of both aircraft transverse field components near the center of the storm, where the tracks cross, suggests a positive charge center below both aircraft in the region. A similar reversal occurs near ($X = 14$, $Y = -30$) along the T-28 track, consistent with another positive center below the aircraft there.

The vertical positions of lightning dipole and monopole solutions at this time (Fig. 5d) are consistent with negative charge regions above both aircraft but do not preclude positive charge regions below. Recall also that only one-half of all lightning events detected by the field mill network could be resolved into dipole or monopole solutions in this storm. The locations of these solutions for events occurring between 1821 and 1838 (projected onto the *X*–*Y* plane) are shown in Fig. 15.

Particle charge measurements along the P-3 track (Fig. 16) show charges of both signs (Fig. 15a) but predominantly net negative charge (Fig. 15b), with the most negative net values within the central portion of the storm.

To summarize, the electrical observations presented here are consistent with discrete regions of charge associated with individual convective cells within the storm. The observations are, in general, consistent with net negative charge at and above 6.5 km, and positive charge in anvil streaming off the storm to the northwest. The charge distribution becomes more complex as the storm evolves.

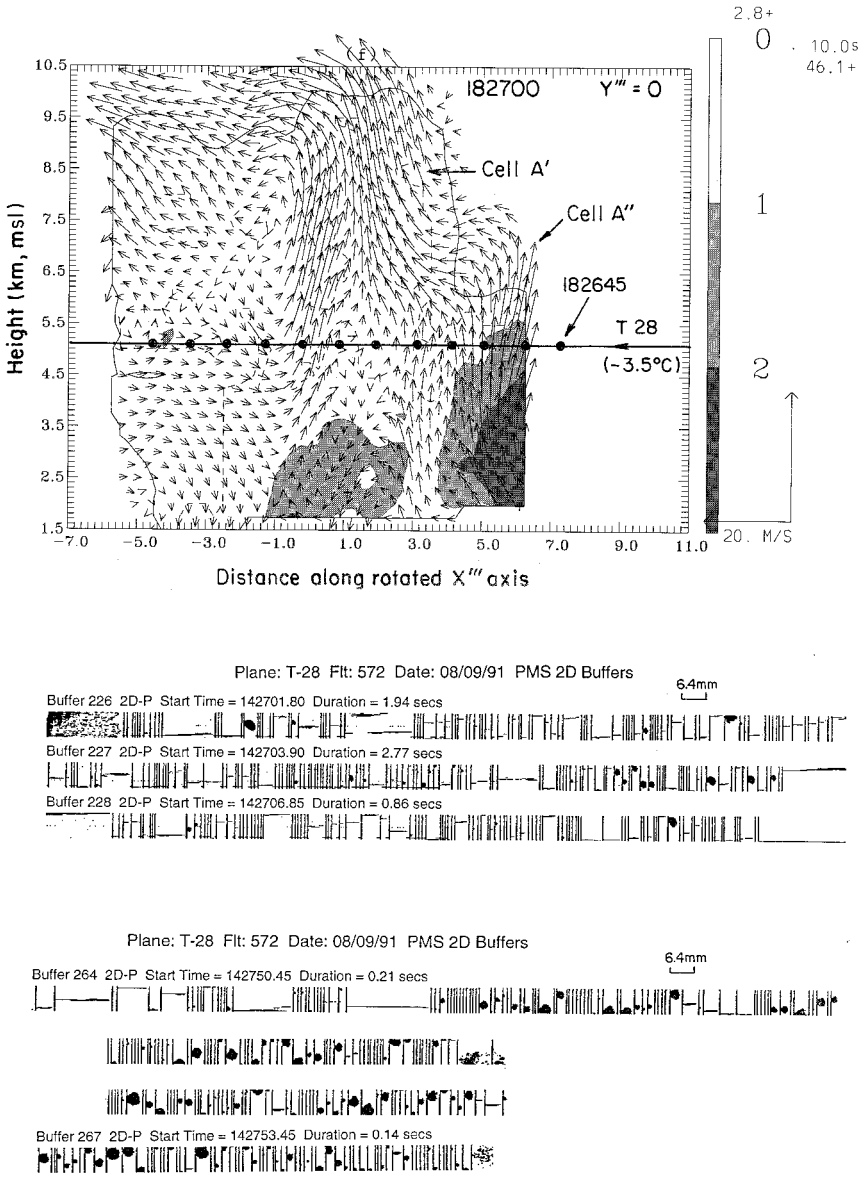

FIG. 14. (*Continued*) (f) As in Fig. 6f except vertical section along the T-28 track or $Y''' = 0$ cut plane (see Fig. 3g for origin and orientation of X''', Y''' axes). The updraft sector marked AB in panel (a) is near 1827:00 UTC which corresponds to cell A″. The 2D precipitation probe images from T-28 at (g) 1427:02–1427:07 (within updraft sector marked AB in panel (a), and (h) 1427:50–1427:53. Note local daylight times (add 4 h for UTC).

Late in the evolution of the storm, observations are consistent with positive charge below 5 km.

7. Discussion

This multicell storm consisted of five major cells, the history of three of which were discussed in detail in section 5 (cells B, A, and D). Two additional cells (C and E) in Figs. 3b–d were also analyzed in a similar manner (but details are not shown here). A number of parameters characterizing the various cells are shown in Table 2. In many ways the convective cells in this storm resembled those analyzed by Yuter and Houze (1995a,b) in their CaPE study. Cell sizes and lifetimes, the bubble-like nature of the convection, the distinct Z_{DR} columns appearing only in those cells formed early in the storm life cycle, and the strong up- and downdraft couplets in the upper regions of the storms were characteristics observed in both their studies and ours. However, during the growth phase of all cells considered here, updrafts and Z_{DR} columns were virtually coincident, contrary to the pattern observed by Yuter and Houze (1995b).

Each cell displayed a positive Z_{DR} column whose

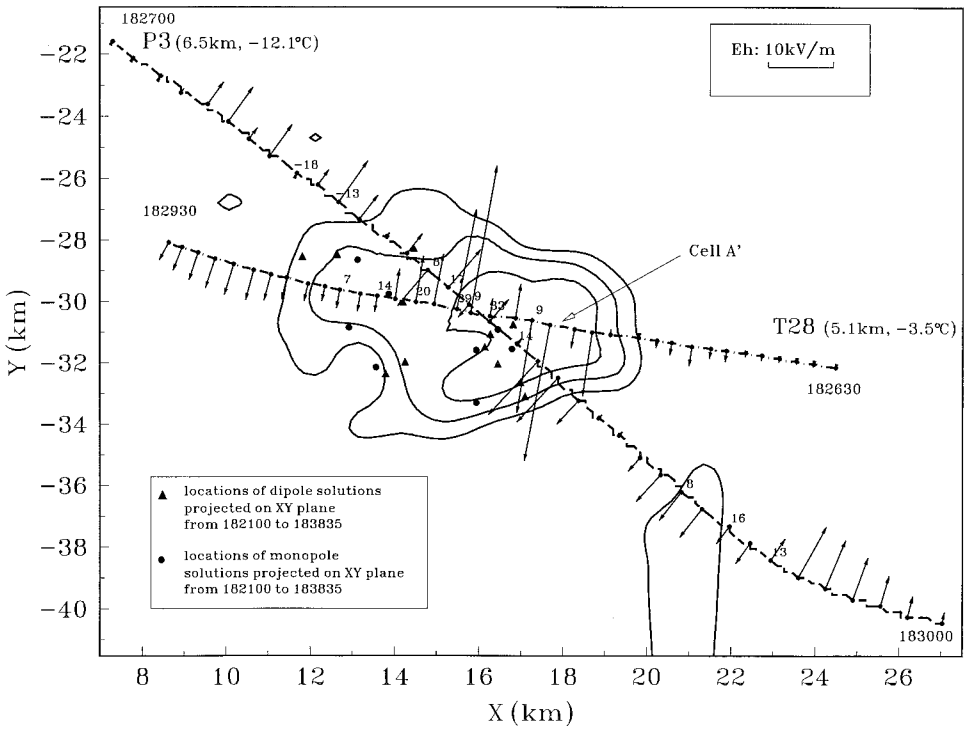

FIG. 15. As in Fig. 12, except for the period 1827–1829 UTC. Vertical field components ($|E_z|$) exceeding 5 kV m^{-1} are shown.

character is described by the maximum value of Z_{DR} attained at 5.5 km (−6.5°C), as well as the vertical extent of the 1.5-dB Z_{DR} contour. The Z_{DR} columns of cells A, B, and D are in this sense ''stronger'' than in cells C and E. Raindrops with reflectivity-weighted diameters of 4 mm (corresponding to $Z_{DR} = 2.6$ dB) were likely present in cells A, B, and D at the −6.5°C level in peak concentrations of approximately 35 m^{-3}, 1 m^{-3}, and 5 m^{-3}, respectively (Jameson 1983). Raindrop freezing was accompanied by enhanced LDR and, for sufficiently large concentrations, enhanced A_3. Only cell A displayed enhanced A_3 values at 5.5-km height. Typically, the updraft continued to accelerate above this level, even as freezing continued, and then downdraft began to appear at middle levels and propagate downward on the downshear edges of the updrafts.

The updraft area was largest for cell A (at about 9 km^2), whereas the other cells were nearly comparable (2–3 km^2) in area. Cells A, B, and D had a larger w at higher altitudes compared to C and E, consistent with the ''stronger'' positive Z_{DR} columns for A, B, and D. Cell A had the largest areal extent and largest peak w and was the only cell with $Z_h > 50$ dBZ at 5.5-km height. It had a peak IWC of a factor of two greater than the other cells. Its 20-dBZ echo tops reached 9.5 km, but this parameter by itself does not capture the strength of cell A since cells D and E also reach 9 km but were much weaker. Table 2 thus shows that cell A was the most active of the convective regions in the storm in terms of updraft magnitude, areal extent, and precipitation production. Cell D was the next strongest with strong updrafts (18 m s^{-1}) at a higher altitude (6.3 km) relative to cell A but did not develop as much precipitation mass due to smaller size and shorter lifetime. The weaker cells (B, C, and E) are overall nearly comparable to each other.

Cell B was the first one detected by radar (at 1748) and appeared to have an active coalescence process well before the first strong updraft pulse at 1758 (see Table 1). The ice phase was most likely initiated by the freezing of drizzle and raindrops. Beard (1992) suggests that the freezing of raindrops is the dominant mechanism by which ice first appears in clouds with an active coalescence process below the freezing level, because, among all cloud particles, raindrops will have the highest probability per unit time of encountering freezing nuclei active at relatively high temperatures. Within a few (~5) minutes after the first updraft pulse at 1758, cell B glaciates at 1803 (see Table 1), and its upper level tilts to the northwest. Because cells A and D are located northwest of cell B (Fig. 3b), ice from cell B could have been introduced into these cells via horizontal flow and upper-level downdraft between cells (Figs. 3b,b′). However, freezing of drizzle and rain within cells A and D would likely have been important sources of ice in these cells, too.

Conditions were suitable for subsequent development of ice particles in all cells by a variety of processes.

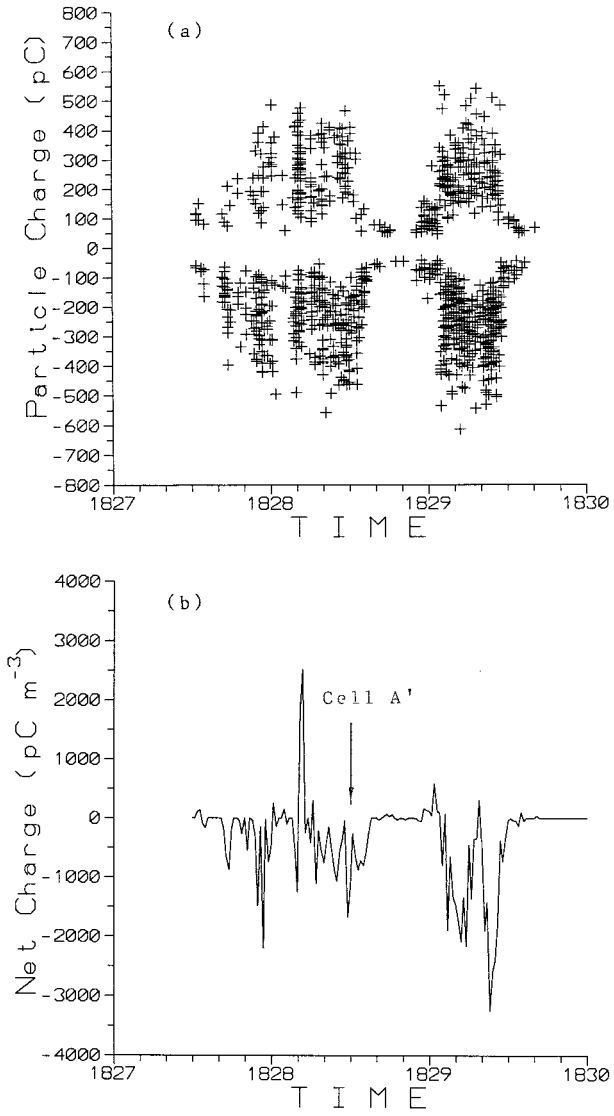

FIG. 16. As in Fig. 15 except for the period 1827–1829 UTC. Beyond 1829, the charges are from another storm (not analyzed here).

The net effect was significant concentrations (hundreds per liter) of ice particles detected by the aircraft in downdrafts bringing particles from higher levels to the 5–6-km level, ranging from millimeter graupel to the smallest sizes detectable by aircraft probes (roughly 50 μm). These high concentrations were found even during the dissipating stage of cell B, which was not significantly electrified. Peak total precipitation particle number concentrations at midlevels, as measured by PMS 2D probes on the various aircraft, were similar (to within an order of magnitude) between the cells. The size spectra decreased exponentially with increasing size, meaning that similarity in number concentration was due mostly to similarity in concentration of particles less than 0.5 mm in maximum dimension. The concentration of the drops and graupel particles larger than roughly 3 mm was higher in cells A and D, which were more vigorous and persistent and which became more strongly electrified. Comparing the size spectra from the final penetrations of cells D and A, there is an increase in peak size present in measurable concentrations from approximately 2 mm (cell D, Fig. 11a) to 3 mm (old part of cell A, Fig. 14d) to 4 mm (new part of cell A, Fig. 14d). This progression correlates with the increasing electric fields measured by penetrating aircraft at midlevels. Only cell A (and A′) developed detectable lightning.

Prior work (e.g., Dye et al. 1986; Dye et al. 1989; Goodman et al. 1988; Weinheimer et al. 1991; Willis et al. 1994) suggests that electrification is related to higher concentrations and broader precipitation spectra in the temperature range ($-5°$ to -20°C). Comparing the time–height cross sections in Figs. 5 (cell A) and 7 (cell D), the peak reflectivities above 7-km altitude exceed 30 dB*Z* for 20 min in cell A, whereas they only briefly exceed 30 dB*Z* in cell D. In situ observations in downdraft regions in the 5–6-km altitude region suggest that 30-dB*Z* echo above 7 km is an indication, in these cells, of a broad spectrum of ice crystals and graupel particles. In situ observations of cloud water are not available above 6.5 km (-12°C). At 6.5 km, however, cloud water greater than 1 g m^{-3} was present in the updrafts through the early to mature stages of the convective elements, and it is reasonable to assume that some persisted to 7 km in the stronger updrafts, at least until precipitation development resulted in its scavenging. Thus, both radar observations in the upper cloud region and in situ observations at midlevels support the correlation between broad ice particle spectra, cloud water, and stronger electrification.

Electric field measurements are consistent with charge distributed in a horizontally cellular manner within the storm, with distinct negative charge centers associated with each of the convective elements in cells A and D. This type of distribution has also been observed using aircraft measurements in New Mexico clouds (Breed and Dye 1989) and presents a picture of charge distribution somewhat different than (but not necessarily inconsistent with) that derived from vertical balloon soundings in very large thunderstorms and thunderstorm complexes in the High Plains (see, e.g., Marshall et al. 1995).

The peak vertical electric field components at midlevels were sensed, not in the developing updraft regions, but in downdraft, and in transition regions between updraft and downdraft, where graupel was descending from above. The simplest interpretation of the electric field and lightning field change observations, up to the period when lightning began, is that net negative charge accompanied graupel as it descended through 7 km to the aircraft penetration levels.

The inferred major net negative charge layer near 7–8-km altitude in this storm is in the altitude range where it has been deduced in many other storm studies in many

regions of the world, based on field changes due to lightning (e.g., Williams 1989). The net negative charge was observed at lower altitudes but at similar temperatures, compared to the net negative charge region found by direct measurement of charge on graupel in a vigorous New Mexico thunderstorm discussed by Weinheimer et al. (1991).

During flight under anvil in clear sky, or in light precipitation, the dominant vertical field component was negative, consistent with positive charge in this cloud-top region.

These observations also show the very rapid development of electrification in cells A and D, from negligible fields and no lightning, to fields of the order of 10 kV m^{-1} in the 5.3–6.5-km altitude range within 4–5 min. This time interval is similar to those observed for electrification in other Florida clouds during CaPE (Willis et al. 1994; Ramachandran et al. 1996; French et al. 1996; Jameson et al. 1996) and in more continental thunderstorms (e.g., Dye et al. 1986; Breed and Dye 1989). In cell A the time from the appearance of the first reflectivity greater than 35 dB*Z* associated with graupel (as inferred from first radar returns above this magnitude from above 6-km altitude) to the first lightning is about 6 min, compared to 8 min in the Montana storm discussed by Dye et al. (1986).

The criteria for electrification (as indicated by in situ electric fields greater than 1 kV m^{-1}) established for a sample of New Mexico thunderstorms in Dye et al. (1989) is reflectivities greater than 40 dB*Z* at 6 km (~ -8°C) and echo tops higher than about 8 km. These same criteria fit well cells A and D in the Florida storm we studied. Despite the active coalescence precipitation process early in the development of the Florida storms, it appears that electrification is most strongly correlated with development of the ice-phase precipitation process as cloud tops grow above 8 km and apparently in much the same pattern as in more continental thunderstorms with a much less important coalescence process.

8. Summary

Observations of this small multicell thunderstorm have yielded quantitative descriptions of storm kinematic, microphysical, and electric fields in individual convective cells as they develop, mature, and decay. During an active convective period of about 50 min, five major cells having lifetimes ranging from 10 to 20 min developed within the storm. The most significant cell exhibited three consecutive development cycles (cell A followed by A′ and A″). The updrafts in this storm were 2–4 km wide and went through a bubble-like evolution, with updraft maxima rising with time. Peak vertical winds in the strongest updrafts were about 20 m s^{-1}. First radar echoes generally occurred below the freezing level. A differential reflectivity (Z_{DR}) ''column'' extending above the freezing level, characterized by high Z_{DR} and low *Z*, indicating regions containing low concentrations of millimeter-size raindrops, was associated with each cell during its developing stages. This column reached altitudes exceeding 6 km (-8°C) in the stronger updrafts. As the Z_{DR} columns reached maximum altitude, a ''cap'' of enhanced linear depolarization ratio (LDR) and enhanced 3-cm-wavelength attenuation (A_3) formed, overlapping the upper regions of the Z_{DR} column. These parameters indicated development of mixed-phase conditions in these regions as the supercooled raindrops began to freeze.

Aircraft observations in the 4–6.5-km altitude range documented the development of larger and more precipitation in the central convective cell, compared to cells on the storm periphery. This cell also developed an order of magnitude more radar-estimated precipitation than did the other cells. Peak particle diameters of 5–6 mm were found by aircraft instrumentation in the strongest cells at all penetration levels, with smaller peak diameters in the weaker cells. Peak cloud liquid water concentrations at midlevels were 3 g m^{-3} or less, far less than adiabatic values at these altitudes, indicating that adiabatic cloud water concentrations, if they did develop, probably only occupied small volumes of a cell for short periods of time. The highest cloud water concentrations were found in updrafts accompanied by low concentrations of large raindrops. The raindrops were freezing in some cases. The highest precipitation particle concentrations were found in regions of graupel in midlevel downdrafts, accompanied by cloud water concentrations less than a few tenths of grams per cubic meter.

Only the central and strongest convective cell developed lightning. Electric fields exceeding 10 kV m^{-1} were noted during aircraft penetrations in this as well as several other cells that did not produce lightning. Fields exceeding 1 kV m^{-1} were noted by the instrumented aircraft at midcloud levels within minutes of the radar-indicated development of mixed-phase conditions at these levels or aloft. The first intracloud lightning was detected in observations of the surface field mill network within 6 min of development of mixed phase conditions aloft in the first cycle of development in the central cell, with the first cloud-to-ground event noted within 9 min of this development. Lightning continued through two additional cycles of updraft growth in this central region and diminished as the convection diminished after approximately 30 min.

Aircraft-measured electric fields and lightning retrievals from the surface field meter network are consistent with a tendency for negative charge to accumulate above the 6.5-km (-12°C) level within regions of radar reflectivity maxima and for positive charge to accumulate in the anvil region well above 9 km (-30°C) and below 5.1 km (-3°C) later in the storm life cycle. A charge-detecting induction ring device on the P-3 consistently found charges of both signs present as it penetrated at 6.5 km (-12°C), with a net negative total charge.

Acknowledgments. VNB, LL, and IJC acknowledge support from the NSF via Grants ATM-9014600 and ATM-9410698 to CSU. Both LL and IJC were at CSU during the major period of this work. KK acknowledges support from the NSF via 9200667 to UAH, while AD acknowledges support via ATM-9022846 and ATM-9509810 and via cooperative agreements ATM-9104474 and 9401117 to SDSM&T. Mr. Ken Hartmann of SDSM&T assisted greatly with the PMS data processing from all the aircraft. Mr. M. Murphy and Dr. P. Krider graciously provided the surface field mill network analysis results. Particle charge data from the P-3 were provided by Dr. Ian Brooks. The authors acknowledge the assistance rendered by Drs. Paul Smith, Dennis Musil, and Jim Fankhauser and by Mr. Dan Breed. The Atmospheric Environment Service of Canada provided the 2D-P probe and New Mexico Tech provided some of the field mills for the T-28. The National Center for Atmospheric Research provided the REORDER and CEDRIC software used in the radar analysis.

APPENDIX A

Radar Analysis Procedures

a. Doppler analysis procedure

The wind field synthesis of 15 volumes was completed using standard methodology consisting of raw data editing (using the NCAR RDSS software), interpolation of velocity, and reflectivity factor to a three-dimensional grid using the NCAR REORDER software, and subsequent synthesis of the three velocity components in the Cartesian space used the NCAR CEDRIC software (Miller et al. 1986). During the editing process, particular effort was taken to remove radial velocity contributions resulting from (a) three-body scatter events (the so-called flare echo as defined by Wilson and Reum 1988), which were present on the far side of reflectivity cores in the C-band (CP-3 and CP-4) data during the intense storm stages, and (b) various point outliers including aircraft and ground clutter contamination.

A relatively fine grid having 250-m horizontal and 500-m vertical spacing was used to produce a minimum resolvable scale of about 2 km (at 50% amplitude). The interpolation with the NCAR REORDER software used a Cressman weighting scheme with a 0.5-km horizontal radius and a 0.7–0.9-km vertical radius. The range to storm core for all radars was 28–38 km during the period of analysis.

Two filtering applications involving a Leise (1981) two-dimensional filter were then applied, the first on the radial velocity fields prior to the wind field synthesis, and the second on the u, v wind components prior to the calculation of divergence. The u, v wind components were obtained from a least-squares formulation of radial velocity data from three radars (CP-2, CP-3, and CP-4). Vertical motion was obtained from integration of the divergence field using a variational technique to satisfy upper and lower boundary conditions. The vertical motion in this case is thought to be accurate within 2–4 m s^{-1}. Intercomparison of peak updraft from the Doppler analysis with aircraft measurements along selected penetrations shows good agreement to within about ± 4 m s^{-1}. The multiple Doppler scan times are as in Table A1.

TABLE A1. Multiple Doppler scan times.

Time (UTC)	CP-2	CP-3	CP-4
1750		1750:05–1751:46	1750:05–1752:48
1752	1751:15–1753:20	1752:27–1754:01	1753:01–1753:11
1755	1754:37–1756:37	1756:03–1757:43	1755:52–1756:43
1758	1757:45–1759:48	1758:17–1759:58	1758:31–1759:46
1801	1801:38–1803:40	1800:52–1802:54	1800:50–1803:13
1804	1803:46–1805:17	1803:00–1805:06	1803:26–1805:47
1808	1807:32–1808:57	1807:27–1809:34	1807:38–1810:00
1810	1809:03–1811:06	1809:47–1811:54	1810:13–1812:36
1815	1814:48–1816:23	1814:15–1816:35	1814:26–1816:43
1817	1816:30–1818:07	1816:44–1819:04	1816:58–1819:15
1821	1821:44–1823:22	1820:58–1823:18	1821:09–1823:17
1824	1823:27–1825:05	1823:28–1825:48	1823:40–1825:56
1828	1827:14–1829:01	1827:40–1829:41	1827:50–1830:27
1830	1829:07–1830:54	1829:52–1831:53	1830:41–1833:18
1835	1834:24–1835:56	1834:50–1837:25	1835:01–1837:37

b. Multiparameter radar analysis

The CP-2 multiparameter radar is described in Bringi and Hendry (1990). The raw data from the radar consists of range profiles of horizontally polarized reflectivity (Z_h), differential reflectivity (Z_{DR}), linear depolarization ratio at X-band (LDR), and the dual-frequency reflectivity ratio (DFR) from the two frequencies (S and X bands). These data were filtered in range using a ''light'' infinite impulse response filter that strongly attenuates (>20 dB) spatial-scale fluctuations of less than or equal to 250 m, while fluctuations on the order of 500 m and above are passed through (Hubbert et al. 1993). From the range profiles of DFR, the specific attenuation at X band A_3 (dB km^{-1}) is derived using an ''adaptive'' filtering technique described by Hubbert and Bringi (1995). The accuracy in estimating A_3 is around 0.25–0.5 dB km^{-1}. The accuracy in estimates of Z_h (± 1 dB) and Z_{DR} (± 0.25 dB) are standard (see Doviak and Zrnić 1993).

Once the derived parameters such as A_3 and LDR (corrected for propagation effects) are computed at each range resolution volume, the multiparameter set (Z_h, Z_{DR}, A_3, and LDR) are interpolated onto a Cartesian grid using the NCAR REORDER software package. A relatively fine grid spacing was used (250 m in the three directions). A Cressman weighting scheme was used with 250-m horizontal radius and 500-m vertical radius (for volume data acquired in PPI mode); for data in rhi mode the horizontal radius was set to 500 m and vertical radius to 250 m. The gridded multiparameter data were

TABLE A2. Cartesian boxes for cell B.

Volume	Center time (UTC) of scan	Time (s)	X_{min} (km)	X_{max} (km)	Y_{min} (km)	Y_{max} (km)
v119	1748:45	0	11.0	14.0	−29.0	−25.0
v121	1752:17	212	11.0	14.0	−29.0	−26.0
v123	1755:35	410	12.0	15.5	−30.0	−26.5
v125	1758:46	601	13.0	17.0	−31.0	−27.0
v126	1800:43	718	14.0	17.0	−31.5	−28.0
v127	1802:38	833	14.0	18.0	−31.5	−28.0
v128	1804:30	946	15.0	18.0	−32.0	−28.0
v129	1806:24	1059	15.0	18.0	−32.0	−28.0
v130	1808:14	1169	15.5	18.5	−32.0	−28.4

then merged with the gridded Doppler data yielding at each grid point the variables Z_h, Z_{DR}, LDR, A_3, and cell-relative wind components u_r, v_r, and w. The NCAR CEDRIC software was then used to further analyze and display the composite fields.

Other derived parameters such as ice water content (IWC) and liquid water content (LWC) were obtained using the difference reflectivity method (Golestani et al. 1989; Doviak and Zrnić 1993; Chandrasekar et al. 1991). Without going into details here (see Doviak and Zrnic 1993), a ''fraction'' of ice parameter can be computed at each grid point, which is the ratio of Z_h^i/Z_h, where Z_h^i is the reflectivity due to ice particles alone and Z_h is the total reflectivity (sum of ice and rain components). An empirical equation (Sikdar et al. 1974) for liquid water content is used here at each grid point,

$$\text{LWC} = 3.93 \times 10^{-3}[(1 - f)Z_h]^{0.549} \text{ (g m}^{-3}\text{)},$$

where Z_h is in its standard units (mm^6 m^{-3}). The ice water content at each grid point obtained from

$$\text{IWC} = 3.93 \times 10^{-3}(4.335fZ_h^i)^{0.549} \text{ (g m}^{-3}\text{)}$$

The rainfall rate (mm h^{-1}) is computed from (Jameson 1992)

TABLE A3. Cartesian boxes for cell A.

Volume	Center time (UTC) of scan	Time (s)	X_{min} (km)	X_{max} (km)	Y_{min} (km)	Y_{max} (km)
v128	1804:30	0	11.5	14.0	−28.1	−26.4
v129	1806:28	118	12.0	14.0	−28.6	−25.6
v130	1808:15	225	12.0	15.0	−30.0	−26.4
v131	1810:08	338	11.5	15.0	−30.0	−26.0
v132	1812:05	455	11.5	16.0	−30.5	−26.0
v133	1813:53	563	12.0	16.0	−31.0	−26.0
v134	1815:36	666	12.0	17.0	−31.0	−26.0
v135	1817:18	768	12.0	17.0	−32.0	−26.5
v136	1819:01	871	12.0	18.0	−32.0	−27.0
v137	1820:47	977	12.0	18.0	−32.0	−27.0
v138	1822:32	1082	12.0	19.0	−32.0	−27.0
v139	1824:16	1186	13.0	19.0	−33.0	−28.0
v142	1828:07	1417	14.5	22.0	−33.5	−28.5
v144	1831:53	1643	15.0	23.0	−34.0	−29.0
v146	1835:09	1839	16.5	24.5	−34.5	−29.5
v148	1838:36	2046	17.0	24.5	−34.5	−29.5

TABLE A4. Cartesian boxes for cell D.

Volume	Center time (UTC) of scan	Time (s)	X_{min} (km)	X_{max} (km)	Y_{min} (km)	Y_{max} (km)
v128	1804:30	0	11.5	14.0	−26.0	−24
v129	1806:28	118	12.0	14.5	−26.0	−24
v130	1808:15	225	12.0	15.0	−26.2	−24
v131	1810:08	338	12.0	15.0	−26.5	−24
v132	1812:05	455	12.0	15.0	−26.5	−24
v133	1813:53	563	12.0	15.0	−26.0	−24
v134	1815:36	666	12.0	15.5	−26.0	−24

$$R = 54.5(A_3)^{0.845};\ A_3 \geq 0.5 \text{ dB km}^{-1},$$

where A_3 is the (one-way) specific attenuation (dB km^{-1}) at X band and by

$$\text{R} = 0.0107Z_h^{0.91}\ 10^{-0.358Z_{DR}};\ A_3 < 0.5 \text{ dB km}^{-1},$$

where Z_h is in its standard units (mm^6 m^{-3}) and Z_{DR} in decibels.

The coordinates (relative to CP-2 as origin) of the ''boxes'' used in the time–height contours in Figs. 4, 5, and 7 for cells B, A, and D, respectively, are given in Tables A2, A3, and A4.

c. Multiparameter data interpretation

A good discussion of multiparameter data interpretation with a large number of references can be found in chapter 8 of Doviak and Zrnić (1993). Good reviews and examples can also be found in Jameson and Johnson (1990) and Herzegh and Jameson (1992). Positive Z_{DR} column interpretations with examples are given in Illingworth et al. (1987), Tuttle et al. (1989), and Bringi et al. (1991). The latter two papers also consider interpretation of A_3 together with Z_{DR}. The dual-frequency (also termed dual-wavelength) method for determining A_3 can be found in Eccles and Mueller (1971); see also Tuttle and Rinehart (1983). Examples of LDR at S band together with aircraft verification has been provided by Frost et al. (1991). Hoeller et al. (1994) provide a good discussion of the microphysical interpretation of multiparameter variables at C band.

APPENDIX B

Summary of Aircraft Instrumentation

The NCAR and Wyoming King Airs, NOAA P-3, and SDSMT T-28 aircraft were all equipped for cloud microphysical and thermodynamic measurements and could also provide estimates of electric fields (except the WKA) and winds (only the vertical wind component, in the case of the T-28). The primary instrumentation used in this study includes PMS (Particle Measuring Systems, Inc.) 2D-P and 2D-C optical array probes, one or both of which were carried by all aircraft, a camera system on the T-28 to photograph precipitation particles in situ (Cannon 1976), PMS King liquid water probes

(except on the T-28), Johnson–Williams cloud water meters, and PMS forward-scattering spectrometer (FSSP) cloud droplet probes. PMS 2D probe data were all processed at SDSM&T using procedures derived from Heymsfield and Parrish (1978) and Detwiler and Hartman (1991). All but the Wyoming King Air carried systems of electric field meters (e.g., Winn 1993), allowing estimates of ambient electric fields at the aircraft position. Ramachandran et al. (1996) describe electric field estimates using the T-28 system. Willis et al. (1994) describe the field meter system on the P-3. The electric field observations used in this study were obtained using prototype observing systems in difficult environments. They were carefully analyzed by workers associated with the individual aircraft involved after they were obtained but cannot be thought of as routine airborne measurements in the same sense as temperature, winds, etc. They can be considered to be correct in sign and accurate to within a factor of 2 in magnitude to the best of our current understanding.

Aircraft positions were obtained using GPS receivers on the Wyoming King Air and T-28, Federal Aviation Administration (FAA) ARTCC radar tracking information for all aircraft, and inertial navigation systems on all but the T-28. Aircraft positions relative to radar reflectivity patterns were verified by periodically detecting echoes due to the aircraft.

Additional details concerning the configuration of the aircraft as flown in CaPE are given in the CaPE data summary (Williams et al. 1992).

REFERENCES

Beard, K. V., 1992: Ice initiation in warm-base convective clouds: An assessment of microphysical mechanisms. *Atmos. Res.,* **28,** 446–450.

Blanchard, D. C., 1957: Supercooling, freezing and melting of giant waterdrops in air. *Artificial Stimulation of Rain, Proceedings of First Conference on the Physics of Cloud and Precipitation Particles*, Pergamon Press, 233–249.

Breed, D. W., and J. E. Dye, 1989: The electrification of New Mexico thunderstorms. 2. Electric field growth during initial electrification. *J. Geophys. Res.,* **94,** 14 841–14 854.

Bringi, V. N., and T. A. Seliga, 1977: Scattering from axisymmetric dielectrics or perfect conductors imbedded in an axisymmetric dielectric. *IEEE Trans. Antennas Propag.,* 575–580.

——, and A. Hendry, 1990: Technology of polarization diversity radars for meteorology. *Radar in Meteorology,* D. Atlas, Ed., Amer. Meteor. Soc., 153–190.

——, D. A. Burrows, and S. M. Menon, 1991: Multiparameter radar and aircraft study of raindrop spectral evolution in warm-based clouds. *J. Appl. Meteor.,* **30,** 853–880.

——, I. J. Caylor, J. Turk, and L. Liu, 1993: Microphysical and electrical evolution of a convective storm using multiparameter radar and aircraft data during CaPE. Preprints, *26th Int. Conf. on Radar Meteorology,* Norman, OK, Amer. Meteor. Soc., 312–314.

——, K. Knupp, and L. Liu, 1995: Microphysical and kinematic study of early-to-mature cloud transition using multiparameter radar, dual-Doppler synthesis and aircraft penetrations. Preprints, *Conf. on Cloud Physics,* Dallas, TX, Amer. Meteor. Soc., 267–271.

——, L. Liu, P. C. Kennedy, V. Chandrasekar, and S. A. Rutledge, 1996: Dual multiparameter radar observations of intense convective storms: The 24 June 1992 case study. *Meteor. Atmos. Phys.,* **59,** 3–31.

Brooks, I. M., 1993: Laboratory studies of thunderstorm charging processes. Ph.D. dissertation, University of Manchester, 164 pp. [Available from Physics Department, UMIST, Sackville St., Manchester, M60 1QD United Kingdom.]

Byers, H. R., and R. R. Braham Jr., 1949: *The Thunderstorm.* U.S. Govt. Printing Office, 287 pp.

Cannon, T. J., 1976: A particle camera for powered aircraft. Preprints, *Int. Conf. on Cloud Physics,* Boulder, CO, Amer. Meteor. Soc., 572–575.

Chandrasekar, V., C. A. Atwater, and T. H. V. Haar, 1991: Convective latent heating estimates from radar data. *25th Int. Conf. on Radar Meteorology,* Paris, France, Amer. Meteor. Soc., 155–158.

Detwiler, A. G., and K. R. Hartman, 1991: IAS Method for 2D Data Analysis on PC's. Institute of Atmospheric Sciences, Report SDSMT/IAS/B91-5, 37 pp. [Available from South Dakota School of Mines and Technology, Rapid City, SD 57701.]

Doviak, R. J., and D. S. Zrnić, 1993: *Doppler Radar and Weather Observations.* Academic Press, 562 pp.

Dye, J. E., J. J. Jones, W. P. Winn, T. A. Cerni, B. Gardiner, D. Lamb, R. L. Pitter, J. Hallett, and C. P. R. Saunders, 1986: Early electrification and precipitation development in a small, isolated Montana cumulonimbus. *J. Geophys. Res.,* **91,** 1231–1247.

——, W. P. Winn, J. J. Jones, and D. W. Breed, 1989: The electrification of New Mexico thunderstorms. 1. Relationship between precipitation development and the onset of electrification. *J. Geophys. Res.,* **94,** 8643–8656.

Eccles, P. J., and E. A. Mueller, 1971: X-band attenuation and liquid-water content estimation by a dual-wavelength radar. *J. Appl. Meteor.,* **10,** 1252–1259.

French, J. F., J. H. Helsdon, A. G. Detwiler, and P. L. Smith, 1996: Microphysical and electrical evolution of a Florida thunderstorm. Part I: Observations. *J. Geophys. Res.,* **101,** 18 961–18 977.

Frost, I. R., J. W. F. Goddard, and A. J. Illingworth, 1991: Hydrometeor identification using cross polar radar measurements and aircraft verification. Preprints, *25th Int. Conf. on Radar Meteorology,* Paris, France, Amer. Meteor. Soc., 658–661.

Golestani, Y., V. Chandrasekar, and V. N. Bringi, 1989: Intercomparison of multiparameter radar measurements. *Preprints, 24th AMS Conf. on Meteorology,* Tallahassee, FL, Amer. Meteor. Soc., 309–314.

Goodman, S. J., D. E. Buechler, P. D. Wright, and W. D. Rust, 1988: Lightning and precipitation history of a microburst-producing storm. *Geophys. Res. Lett.,* **15,** 1185–1188.

Herzegh, P. H., and A. R. Jameson, 1992: Observing precipitation through dual-polarization radar measurements. *Bull. Amer. Meteor. Soc.,* **73,** 1365–1374.

Heymsfield, A. J., and J. L. Parrish, 1979: Techniques employed in the processing of particle size spectra and state parameter data obtained with the T-28 aircraft platform. NCAR Tech. Note NCAR/TN-137&IA, 78 pp. [Available from National Center for Atmospheric Research, Boulder, CO 80303.]

Hoeller, H., V. N. Bringi, J. Hubbert, M. Hagen, and P. F. Meischner, 1994: Life cycle and precipitation formation in a hybrid-type hailstorm revealed by polarimetric and Doppler radar measurements. *J. Atmos. Sci.,* **51,** 2500–2522.

Hubbert, J., and V. N. Bringi, 1995: An iterative filtering technique for the analysis of copolar differential phase and dual-frequency radar measurements. *J. Atmos. Oceanic Technol.,* **12,** 643–648.

——, and ——, 1996: Specular null polarization theory: Applications to radar meteorology. *Trans. IEEE Geosci. Remote Sens.,* **34,** 859–873.

——, V. Chandrasekar, and V. N. Bringi, 1993: Processing and interpretation of coherent dual-polarized radar measurements. *J. Atmos. Oceanic Technol.,* **10,** 155–164.

Illingworth, A. J., 1988: The formation of rain in convective clouds. *Nature,* **336,** 754–756.

——, J. W. F. Goddard, and S. M. Cherry, 1987: Polarization radar

studies of precipitation development in convective storms. *Quart. J. Roy. Meteor. Soc.,* **113,** 469–489.

Jameson, A. R., 1983: Microphysical interpretation of multiparameter radar measurements in rain. Part I: Interpretation of polarization measurements and estimation of raindrop shapes. *J. Atmos. Sci.,* **40,** 1792–1802.

——, 1992: The effect of temperature on attenuation correction schemes in rain using polarization propagation differential phase shift. *J. Appl. Meteor.,* **31,** 1106–1118.

——, and D. B. Johnson, 1990: Cloud microphysics and radar. *Radar in Meteorology*, D. Atlas, Ed., Amer. Meteor. Soc., 323–340.

——, M. J. Murphy, and E. P. Krider, 1996: Multiple parameter radar observations of isolated Florida thunderstorms during the onset of electrification. *J. Appl. Meteor.,* **35,** 343–354.

Johnson, D. B., 1987: On the relative efficiency of coalescence and riming. *J. Atmos. Sci.,* **44,** 1671–1680.

Knupp, K. R., 1987: Downdrafts within High Plains cumulonimbi. Part I: General kinematic structure. *J. Atmos. Sci.,* **44,** 987–1008.

Leise, J. A., 1981: A multidimensional scale-telescoped filter and data extension package. NOAA Tech. Memo. ERL WPL-82, 20 pp. [Available from NOAA/ERL/ETL, 325 Broadway, Boulder, CO 80303.]

Mardia, K. V., 1972: *Statistics of Directional Data*. Academic Press, 357 pp.

Marshall, T. C., W. D. Rust, and M. Stolzenburg, 1995: Electrical structure and updraft speeds in thunderstorms over the southern Great Plains. *J. Geophys. Res.,* **100,** 1001–1014.

Miller, L. J., C. G. Mohr, and A. J. Weinheimer, 1986: The simple rectification to Cartesian space of folded radial velocities from Doppler radar sampling. *J. Atmos. Oceanic Technol.,* **3,** 143–161.

Murphy, M. J., E. P. Krider, and M. W. Maier, 1996: Lightning charge analyses in small Convection and Precipitation Electrification (CaPE) experiment storms. *J. Geophys. Res.,* **101,** 29 615–29 626.

Ramachandran, R., A. Detwiler, J. Helsdon Jr., P. L. Smith, and V. N. Bringi, 1996: Precipitation development and electrification in Florida thunderstorm cells during CaPE. *J. Geophys. Res.,* **101**(D1), 1599–1619.

Rauber, R. M., K. V. Beard, and B. M. Andrews, 1991: A mechanism for giant raindrop formation in warm, shallow convective clouds. *J. Atmos. Sci.,* **48,** 1791–1797.

Sikdar, P. N., R. E. Schlesinger, and C. E. Anderson, 1974: Severe storm latent heat release: Comparison of radar estimate versus numerical experiment. *Mon. Wea. Rev.,* **102,** 455–465.

Smith, P. L., A. G. Detwiler, D. J. Musil, and R. Ramachandran, 1995: Observations of mixed-phase precipitation within a CaPE thunderstorm. *Conf. on Cloud Physics*, Dallas, TX, Amer. Meteor. Soc., 8–13.

Tuttle, J. D., and R. E. Rinehart, 1983: Attenuation correction in dual-wavelength analysis. *J. Climate Appl. Meteor.,* **22**, 1914–1921.

——, V. N. Bringi, H. D. Orville, and F. J. Kopp, 1989: Multiparameter radar study of a microburst: Comparison with model results. *J. Atmos. Sci.,* **46,** 601–620.

Vivekanandan, I., V. N. Bringi, and R. Raghavan, 1990: Multiparameter radar modeling and observations of melting ice. *J. Atmos. Sci.,* **47,** 549–564.

——, J. Turk, and V. N. Bringi, 1991: Ice water path estimation and characterization using microwave radiative transfer techniques. *J. Appl. Meteor.,* **30,** 1407–1421.

——, R. Raghavan, and V. N. Bringi, 1993: Polarimetric radar modelling of mixtures of precipitation particles. *Trans. IEEE Geosci. Remote Sens.,* **31,** 1017–1030.

Vonnegut, B., 1991: How external currents flowing to a thundercloud influence its electrification. *Ann. Geophys.,* **9,** 34–36.

Weinheimer, A. J., J. E. Dye, D. W. Breed, M. P. Spowart, J. L. Parrish, and T. L. Hoglin, 1991: Simultaneous measurements of the charge, size, and shape of hydrometeors in an electrified cloud. *J. Geophys. Res.,* **96,** 20 809–20 829.

Williams, E. R., 1989: The tripolar structure of thunderstorms. *J. Geophys. Res.,* **94,** 298–304.

——, R. Zhang, and J. Rydock, 1991: Mixed-phase microphysics and cloud electrification. *J. Atmos. Sci.,* **48,** 2195–2203.

Williams, S. F., K. Caesar, and K. Southwick, 1992: The convection and precipitation electrification (CaPE) operations summary and data inventory. [Available from NCAR Office of Field Project Support, P.O. Box 3000, Boulder, CO 80307-3000.]

Willis, P. T., J. Hallett, R. A. Black, and W. Hendricks, 1994: An aircraft study of rapid precipitation development and electrification in a growing convective cloud. *Atmos. Res.,* **33,** 1–24.

Wilson, J. W., and D. Reum, 1988: The flare echo: Reflectivity and velocity signature. *J. Atmos. Oceanic Technol.,* **5,** 197–205.

Winn, W. P., 1993: Aircraft measurement of electric field: Self calibration. *J. Geophys. Res.,* **98,** 7351–7365.

Yuter, S. E., and R. A. Houze Jr., 1995a: Three-dimensional kinematic and microphysical evolution of Florida cumulonimbus. Part I: Spatial distribution of updrafts, downdrafts, and precipitation. *Mon. Wea. Rev.,* **123,** 1921–1940.

——, and ——, 1995b: Three-dimensional kinematic and microphysical evolution of Florida cumulonimbus. Part II: Frequency distributions of vertical velocity, reflectivity, and differential reflectivity. *Mon. Wea Rev.,* **123,** 1941–1963.